NAVAL POSTGRADUATE SCHOOL

MONTEREY, CALIFORNIA

THESIS

EFFECTS OF MODULATION SCHEMES ON OPTICAL PULSES TRANSITING AN ELECTROMAGNETICALLY INDUCED TRANSPARENT MEDIUM

by

Christian F. Wachter

September 2023

Thesis Advisor:	Jihane Mimih
Co-Advisor:	Frank A. Narducci

THIS PAGE INTENTIONALLY LEFT BLANK

REPORT DOCUMENTATION PAGE

Form Approved OMB No. 0704-0188

1. AGENCY USE ONLY ***(Leave blank)***	**2. REPORT DATE** September 2023	**3. REPORT TYPE AND DATES COVERED** Master's thesis

4. TITLE AND SUBTITLE EFFECTS OF MODULATION SCHEMES ON OPTICAL PULSES TRANSITING AN ELECTROMAGNETICALLY INDUCED TRANSPARENT MEDIUM	**5. FUNDING NUMBERS**
6. AUTHOR(S) Christian F. Wachter	
7. PERFORMING ORGANIZATION NAME(S) AND ADDRESS(ES) Naval Postgraduate School Monterey, CA 93943-5000	**8. PERFORMING ORGANIZATION REPORT NUMBER**
9. SPONSORING / MONITORING AGENCY NAME(S) AND ADDRESS(ES) N/A	**10. SPONSORING / MONITORING AGENCY REPORT NUMBER**

11. SUPPLEMENTARY NOTES The views expressed in this thesis are those of the author and do not reflect the official policy or position of the Department of Defense or the U.S. Government.

12a. DISTRIBUTION / AVAILABILITY STATEMENT Approved for public release. Distribution is unlimited.	**12b. DISTRIBUTION CODE** A

13. ABSTRACT (maximum 200 words)

This thesis investigates the result of modulation schemes in electromagnetically induced transparency (EIT) in rubidium vapor. Through the process of EIT, a control beam can be used to change the optical properties of a medium experienced by a probe field, generating a transparency window. The corresponding change in index of refraction results in slowed group velocity while the beam propagates through the medium. Modulation is used to transmit a message signal through a medium. In classical systems, this entails converting data into a radio frequency by adding a message to an electronic or optical carrier signal. The properties of EIT, light-slowing, and their impacts on a probe pulse with modulation will be confirmed through a detailed semi-classical analysis and by experimental observation.

14. SUBJECT TERMS electromagnetically induced transparency, light-slowing, modulation	**15. NUMBER OF PAGES** 81
	16. PRICE CODE

17. SECURITY CLASSIFICATION OF REPORT Unclassified	**18. SECURITY CLASSIFICATION OF THIS PAGE** Unclassified	**19. SECURITY CLASSIFICATION OF ABSTRACT** Unclassified	**20. LIMITATION OF ABSTRACT** UU

NSN 7540-01-280-5500

Standard Form 298 (Rev. 2-89)
Prescribed by ANSI Std. 239-18

THIS PAGE INTENTIONALLY LEFT BLANK

EFFECTS OF MODULATION SCHEMES ON OPTICAL PULSES TRANSITING AN ELECTROMAGNETICALLY INDUCED TRANSPARENT MEDIUM

Christian F. Wachter
Captain, United States Marine Corps
BAEM, University of Minnesota, Twin Cities, 2016

Submitted in partial fulfillment of the
requirements for the degree of

MASTER OF SCIENCE IN ELECTRICAL ENGINEERING

from the

NAVAL POSTGRADUATE SCHOOL
September 2023

Approved by: Jihane Mimih
Advisor

Frank A. Narducci
Co-Advisor

Douglas J. Fouts
Chair, Department of Electrical and Computer Engineering

THIS PAGE INTENTIONALLY LEFT BLANK

ABSTRACT

This thesis investigates the result of modulation schemes in electromagnetically induced transparency (EIT) in rubidium vapor. Through the process of EIT, a control beam can be used to change the optical properties of a medium experienced by a probe field, generating a transparency window. The corresponding change in index of refraction results in slowed group velocity while the beam propagates through the medium. Modulation is used to transmit a message signal through a medium. In classical systems, this entails converting data into a radio frequency by adding a message to an electronic or optical carrier signal. The properties of EIT, light-slowing, and their impacts on a probe pulse with modulation will be confirmed through a detailed semi-classical analysis and by experimental observation.

THIS PAGE INTENTIONALLY LEFT BLANK

Table of Contents

THIS PAGE INTENTIONALLY LEFT BLANK

List of Figures

THIS PAGE INTENTIONALLY LEFT BLANK

List of Acronyms and Abbreviations

AOFS	acousto-optic frequency shifter
AOM	acousto-optic modulator
AWG	Arbitrary Waveform Generator
DOD	Department of Defense
DOE	Department of Energy
EIT	electromagnetically induced transparency
EM	electromagnetic
ETAP	Emerging Technology Analytic Panel
IC	integrated circuit
ISR	intelligence, surveillance, and reconnaissance
MIT	Massachusetts Institute of Technology
NPS	Naval Postgraduate School
RWA	rotating wave approximation
^{85}**Rb**	rubidium^{85}
SAS	saturated absorption spectroscopy
SIA	Semiconductor Industry Association
SPIE	Society of Photographic Instrumentation Engineers
QKD	Quantum Key Distribution

THIS PAGE INTENTIONALLY LEFT BLANK

Acknowledgments

To Dr. Mimih and Dr. Narducci, I am deeply indebted to the both of you for the amount of time, energy, and support you have invested in guiding me along this journey. Upon arrival at Naval Postgraduate School (NPS), I knew I wanted to pursue thesis research in a field that is still largely undiscovered, but I was unsure in which direction to go. After some careful thought and prodding for topics, I found Dr. Mimih's academic profile and decided to reach out. Having no idea what to expect in our first meeting, I was delighted to find how patient, knowledgeable, and willing both of you were to assist in identifying and scoping the research into a manageable and well-rewarding experience. Dr. Mimih, I sincerely appreciate the discussions and support in deriving the theoretical framework behind the research. Likewise, Dr. Narducci, I could not have achieved experimental results without your depth of understanding and ingenuity in the lab environment. To both of you, thank you.

To the faculty and staff of the Dept. of Electrical and Computer Engineering, I am eternally grateful for the instruction I received over the past two years at NPS. When I arrived, I was hesitant to begin the rigorous course material required of an engineering degree but quickly realized how truly exceptional and supportive the faculty are. Not only am I more confident in my engineering abilities but I also gained a network of extraordinary academics.

To my wife, Estefania, you are the fuel for my motivation. Without your steadfast support and understanding, I would be a disorganized mess. Thank you from the bottom of my heart for everything you do to support our family and keep us on our feet. We are, and always will be, the best team.

To my parents, thank you for always being present and supportive of my endeavors. Your dependability has always provided a sense of relief and a safety net to fall on. You have shown me how determination and hard work can lead to success; coupled with your support, I cannot fail. Thank you.

Lastly, to anyone who may read this, thank you. It is your turn to take the baton and push further. As Steve Prefontaine once said, "To give anything less than your best, is to sacrifice the gift."

THIS PAGE INTENTIONALLY LEFT BLANK

CHAPTER 1:
Introduction

Quantum technologies offer many advantages over their modern counterparts and have garnered the attention of global superpowers over the past decade. Notably, public investments in 2022 reached unprecedented levels, with China surpassing all other actors in this sector. As reported by [1], the total investment of China has amounted to \$15.3 billion, while the European Union invested \$8.4 billion, and the United States invested \$3.7 billion. In fact, the journal goes on to claim this field shows so much promise that it is expected to aggregate a value of \$1.3 trillion by 2035. And by the year 2040, quantum computing, communication, and sensing are expected to occupy the largest percentages of market share.

Akin to these assertions, the Department of Defense (DOD), Defense Science Board of scientific advisors, acknowledge in the *Defense Primer* report to Congress, quantum sensing, quantum computing, and quantum communication are most likely to benefit the DOD [2]. According to the board, quantum sensing is the most mature of the subcategories and “poised for mission use.” Generally, quantum sensors are characterized by their ability to extend sensing capabilities beyond the traditional limits of classical sensors in terms of precision, accuracy, bandwidth, speed, or other factors such as size, weight, and power. They accomplish this by measuring quantum mechanical phenomena such as spin, coherence, entanglement, or other quantum characteristics. Examples of applications for quantum sensors include alternative position, navigation, and timing protocols impervious to modern GPS-degrading efforts. Additionally, quantum sensors are theorized to enhance the sensitivity of intelligence, surveillance, and reconnaissance (ISR) devices supporting the detection of submarines, underground facilities, and electronic emissions [2].

Quantum communication focuses on using principles of quantum mechanics such as entanglement and superposition to send and receive messages through the transmission of quantum states of light. An important aspect of quantum communication is the protection of information channels by encoding and transmitting data at large distances by allowing stakeholders to share a secure encryption key. Quantum Key Distribution (QKD), for example, is considered one of the most mature applications of quantum communication thus far. The first protocol describing QKD is the BB84 protocol, proposed by Charles H. Bennett and Gilles Brassard in 1984 [3]. This protocol uses polarized photons to create a secure key that is, in principle, secure against any eavesdropping attempt that introduces detectable changes in the error rates introduced by an eavesdropper. Furthermore, the U.S. Department of Energy (DOE) Quantum Information Science Center in collaboration with The University of Chicago has been developing the largest quantum network in the nation and recently completed a 35-mi extension of the communication channels in June, 2022. The extension expands the network to include six nodes and more than 120mi of network communication [4], [5].

Lastly, quantum computing is the least developed of the three, but it leverages similar principles of quantum mechanics to perform certain types of calculations much faster than classical computing. It is an evolving technology with practical challenges in power, data storage, and fault tolerant operations that need to be addressed before widespread commercial use. Reliable quantum-state storage is a ubiquitous trend that appears across many quantum technologies and is the focus of this research. While we continue this research through the lens of computing, we realize that many overlapping fields of study may benefit from its application. For instance, Massachusetts Institute of Technology (MIT) Lincoln Labs, reports in a quantum radar feasibility presentation to Emerging Technology Analytic Panel (ETAP), quantum radar lacks the ability to achieve a *quantum advantage* because current quantum-state storage devices cannot support necessary storage times [6].

1.1 Background

Through the history of computing, consumers have grown more dependent on the high-powered and fast-processing attributes of the modern integrated circuit (IC) to meet throughput demands in an increasingly competitive market. By quick inspection of macroeconomic trends, it is easy to justify the overwhelming reliance and future investment in the IC. As reported by the Semiconductor Industry Association (SIA), “global semiconductor industry sales totaled $574.1 billion in 2022, the highest-ever annual total and an increase of 3.3% compared to the 2021 total of $555.9 billion” [7]. These trends have followed the IC since the invention of the planar silicon transistor in 1959. In fact, six years later, the co-founder of Intel, Gordon Moore, published an article in the 35th anniversary of the *Electronics* magazine that documented an astounding observation. Tasked to predict the legitimacy of the IC in 10 years, Moore looked to chip complexity to tell the story. Gordon explains his revelation in a Society of Photographic Instrumentation Engineers (SPIE) review:

> On a semi-log plot these points fell close to a straight line that doubled the complexity every year up until 1965. To make my prediction, I just extrapolated this line another decade in time and predicted a thousand-fold increase in the number of components in at the most complex circuits available commercially. The cheapest component in 1975 should be one of some 64,000 in a complex integrated circuit. I did not expect much precision in this estimate. I was just trying to get across the idea this was a technology

> that had a future and that it could be expected to contribute quite a bit in the long run [8].

Over time, this well-known straight-line approximation permeated across all semiconductor-related components. Consequently, Moore's Law was born. Fifty years later, Moore's Law continues to hold true in that the number of transistors on a single silicon wafer has nearly doubled every two years. This means more power, faster processing times, and increased productivity for the consumer. However, skepticism exists about the future of Moore's Law and to what limit it may remain true. Furthermore, as manufacturing techniques like enhanced ultra-violet lithography are refined to support angstrom-level precision, understanding the quantum dynamics of the system becomes increasingly necessary. At this scale, the atomic interactions of particles most definitely impact the macro-performance. The academic journal, *Nanotechnology*, is a repository of published cutting-edge work in the field of nanotechnology. In his editorial, Daniel Loss explains, "At the nanoscale, quantum confinement effects dominate the electrical and optical properties of systems. They also render new opportunities for manipulating the response of systems" [9].

However, finding alternatives to classical computing methods have long been explored. In 1980, physicist Richard Feynman of the California Institute of Technology sought to model atomic systems while conducting research. He quickly came to realize that the classical computer did not have the computing capacity to perform such functions. Consider a system of electrons where an electron can be present, or not present, in many different levels of the electron shell. By simple probability there are 2^n possible configurations that require 2^n bits of storage capacity. The memory required quickly exceeds that which is realistic when considering systems of a few hundred electrons; therefore, quantum dynamic simulations on conventional computers may never be efficiently modeled. This realization is often why Dr. Feynman is considered the godfather of Quantum Computing [10].

Quantum storage devices, also termed quantum memory, continue to be an active research topic and critical technology milestone to realize the broad spectrum of quantum technologies. The goal of quantum memory is to map a transmitted signal encoded with a specific sequence of quantum states into a stationary medium where the states are preserved and retrieved later. Through temporary storage and retrieval, quantum memory plays a fundamental role in realization of quantum repeaters which are hypothesized to overcome the loss limitation in optical fibers. Current approaches to quantum memory are classified into three categories: (1) optically controlled memories; (2) engineered absorption; and (3) a hybrid scheme of both combined [11].

This thesis will focus on the most common of the three schemes: optically controlled memory.

There are two prevalent subsets of optically controlled memory, which include electromagnetically induced transparency (EIT) and Raman quantum memory. Here, we will keep our focus on EIT and explore its capabilities and limitations. This type of memory is typically comprised of two optical beams and a storage medium. The first optical beam, termed the *pump*, controls the absorption of the second beam, termed the *probe*, within the storage medium. This storage is possible because the medium has a suitable energy structure that allows for isolation of two ground states and one excited state. A probe beam tuned close to an atomic resonance will be absorbed by the medium. A pump beam tuned close to another atomic transition modifies the absorption of the probe beam in such a way as to reduce the absorption (hence increase transmission) of the probe. In this way, the absorption and transmission of the probe can be controlled optically with the pump beam. The mechanism behind this effect is discussed in Chapter 2. In using this effect, a probe pulse can be stored inside an atomic medium, coherently mapping its quantum information to the particles of the medium, for a finite amount of time.

Now consider a situation in which the storage medium is an integral component of a large quantum information system, transmitting, receiving, and storing data for communication. Through rigorous computations and introduction of a *mixing angle*, work conducted by [12] has shown how the quantum information is mapped to the particles of the storage medium and controlled by an external pump field. Similarly, since information is often transmitted through various modulation schemes, this thesis aims to observe the impact storing a modulated pulse using an EIT scheme may have on the information within the modulation.

1.2 Outline

In the following chapter, we provide a theory behind a semi-classical treatment of EIT as a foundation. We extrapolate from this theory in subsequent sections by applying modulation schemes to the probe field. We seek to understand how the modulation might impact the EIT condition and note the effect on slowed group velocities. Lastly, we develop a theory that can be qualitatively tested in the lab.

In Chapter 3, we introduce experimental procedures to confirm our findings from Chapter 2. Having argued that pulse amplitude modulation may be recovered after transiting the storage medium, it is useful to explore to what extent the medium effects the signal for post-processing procedures, such as error correction coding. We discuss the procedures and techniques used to achieve the EIT effect as well as difficulties.

Chapter 4 provides Experimental results and analysis. Here, EIT is confirmed by measurement of its linewidth under continuous-wave conditions, showing the expected increase in transmission. Then, we introduce a pulse whose frequency spectrum fits within the bandwidth of the transparency window. We provide a demonstration of the light-slowing effect by comparing arrival times of pulses that cross the medium, within and external to, the EIT window. Finally, we add modulation to the pulse and explore the impact on light-slowing.

Finally, we address future work and conclude in Chapter 5.

THIS PAGE INTENTIONALLY LEFT BLANK

CHAPTER 2:
Theory

We begin by exploring an optical phenomenon known as electromagnetically induced transparency (EIT), and specifically how it is manifested in a sample of room-temperature rubidium vapor (and specifically the rubidium^{85} (^{85}Rb) isotope). EIT as its name suggests, is the creation of a transparency window for a probe field near an atomic resonance caused by the application of another field close to a second atomic resonance. The application of the external control field leads to destructive quantum interference of the absorption pathways available to the probe field, thereby eliminating absorption and modifying the dispersion properties inherent to the medium under standard conditions [11].

Rubidium is an ideal candidate to observe EIT for multiple reasons. Rubidium is an alkali metal with a single valence electron and therefore the energy level structure is well understood. Alkali metals exhibit strong interactions with laser fields, allowing for easy control of their internal states. This strong interaction also leads to wide optical transition linewidths allowing for greater error tolerance in the laser frequency fluctuations (e.g., detuning). Greater error tolerance also plays a monetary role; the laser system required to address the most common energy transition in rubidium is relatively cheap as compared to other spectroscopy laser systems. Additionally, in very low-pressure cells (of the kind we use) rubidium experiences very low decoherence rates, which supports the preservation of quantum states and therefore longer information storage times.

The well-known electronic energy structure of rubidium is documented in [13], which conveniently catalogs widely accepted empirical data and provides analysis of the energy level structure of ^{85}Rb. In this section, we briefly review the physics giving rise to fine structure in the energy level structure, as it pertains to later discussions (e.g., [14]). The fine structure is a result of coupling between the orbital angular momentum, $\vec{L}$, of the outer electron and the electron spin angular momentum, $\vec{S}$, of the atom [13]. The total electron angular momentum, $\vec{J}$, is thus

$$\vec{J} = \vec{L} + \vec{S}, \tag{2.1}$$

in which the magnitude of the total angular momentum, J, is bounded by

$$|L - S| \leq J \leq L + S. \tag{2.2}$$

For the purposes of observing EIT, we are interested in the transitions originating from the ground state up to some excited state. Because of selection rules that limit single-photon transitions to changes in angular momentum of $|\Delta L| = 1$ [14], single-photon transitions from the ground state with $L = 0$ can only go to states of orbital angular momentum $L = 1$, the so-called P states. In the ground state, $L = 0$ and $S = 1/2$, and since J can only have positive momentum, $J = 1/2$. However, in the excited state, $L = 1$ and $S = 1/2$, therefore J can assume two possibilities, $J = 1/2$ or $J = 3/2$. These two variations are denoted (for historical reasons) as the D_1 ($5^2S_{1/2} \rightarrow 5^2P_{1/2}$) and D_2 ($5^2S_{1/2} \rightarrow 5^2P_{3/2}$) transitions. The remainder of this paper focuses on the D_2 line transition, as this was the transition used in the experiments. Within the fine structure there exists hyperfine structure, which arises due to interactions between the total angular momentum of the nucleus, $\vec{I}$, with the total angular momentum of the electron, $\vec{J}$ [13]. Then, the total atomic angular momentum is given by

$$\vec{F} = \vec{J} + \vec{I}, \tag{2.3}$$

in which the magnitude of the total atomic angular momentum, F, is bounded by

$$|J - I| \leq F \leq J + I. \tag{2.4}$$

For the ^{85}Rb isotope $I = \frac{5}{2}$. Recalling that in the ground state, $J = \frac{1}{2}$, there are therefore two possible hyperfine levels, $F = 2$ or $F = 3$. In the excited state, $J = \frac{3}{2}$, and thus $F = 1, 2, 3$, or 4.

The two hyper-fine levels of the ground state result in the so-called *Lambda* (Λ) three-level atom energy structure. Due to the various selection rules, a single photon electronic transition between the two ground states is forbidden. The EIT process then involves the two ground states and a single excited state. For the remainder of this thesis, we will employ the notation $|g\rangle$ to refer to the ground state energy level with only fine structure. As we have just discussed, this state is actually degenerate, so we will represent the two states that arise when hyperfine structure is concerned as $|1\rangle$ and $|2\rangle$, with $|1\rangle = |L = 0, S = 0, J = \frac{1}{2}, F = 2\rangle$ and $|2\rangle = |L = 0, S = 0, J = \frac{1}{2}, F = 3\rangle$. Multiple hyperfine levels of the excited state denoted as $|e\rangle$ with only fine structure accounted for are acceptable for use within our experiments (up to selection rules). However, we have chosen to use the $F' = 3$ excited state as the $|3\rangle$ state, as it is the energy level with the largest frequency gap to the nearest excited state. Figure 2.1 provides a visual reference of the D_2 energy structure.

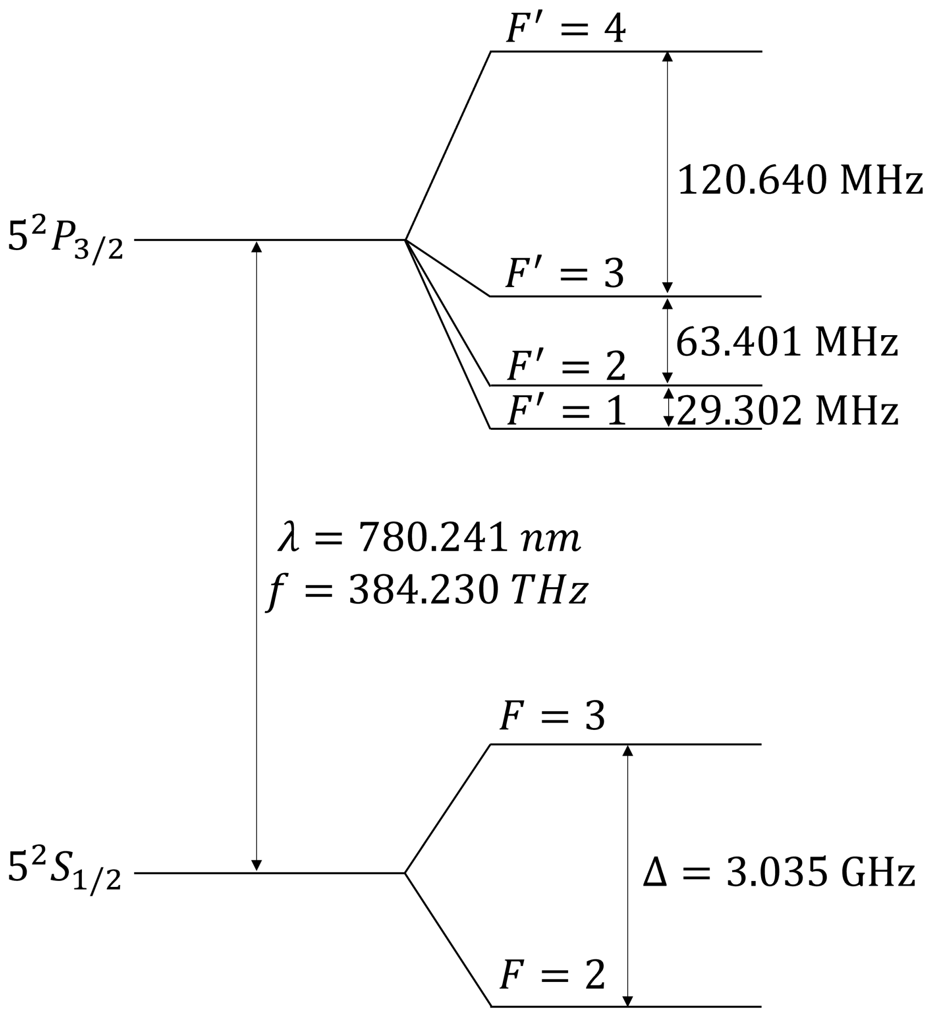

Figure 2.1. ^{85}Rb D_2 transition hyperfine structure, with frequency splittings between the hyperfine energy levels. Adapted from: [13].

2.1 Ordinary EIT of a 3-Level Atom

Understanding energy structure and the possible allowed electronic transitions is an important precursor to investigating EIT. We now examine the quantum dynamics of a closed, 3-level atomic system in the Λ configuration interacting with two laser fields tuned close to the atomic resonances. Multiple mathematical approaches have been documented to describe EIT since original publication of the theory [15] – [17]. In this section, we review one such technique following the formalism described in [18] and [19].

2.1.1 Outline

We begin with a semi-classical approach to the problem of a system of ^{85}Rb atoms in thermodynamic equilibrium (referred to as the storage medium) interacting with two laser fields. The term *semi-classical* is in reference to the specific treatment of the laser fields and ^{85}Rb particles. The electric field of the laser is treated like a classical field whereas the energy level structure of the atom is quantized. The laser fields are applied to the system causing an evolution in the storage medium over time. Specifically, we seek to theoretically describe and experimentally observe the change in absorption and dispersion properties experienced by a probe field caused by the influence of a control field on an atomic medium. The coupling of the two laser fields to their respective transitions (as discussed previously) are depicted in Figure 2.2. We construct a Hamiltonian expression to describe the interaction of an ^{85}Rb particle to the presence of the two fields, which perturb the system. However, the experiments involve the propagation of a probe field through a macroscopic number of particles. Therefore, it is necessary to find an expression that represents the ensemble of particles. We achieve a macroscopic description using the density operator, $\hat{\rho}$. Through a combination of convenient approximations and assumptions we arrive at an understanding of how the electron population density changes over time. In this section, we assume the applied perturbation fields are continuous over all time, enabling calculation of the steady state of the system. Under these conditions, when we consider the full Maxwell wave equation for the fields, we find that the macroscopic polarization is a function of population density. We derive a Beer's Law-like expression for the absorption of the probe field, which is described by the real and imaginary parts of a component of the density operator which is then related to linear susceptibility of the medium. Therefore, by controlling the population density of the system with the control laser through quantum interference, we arrive at a mechanism to alter the index of refraction of the storage medium and thereby control the group velocity of the probe beam.

2.1.2 Derivation

Defining the Hamiltonian

The interaction of a single electron orbiting a single proton (e.g., in a hydrogen atom) is a classic textbook quantum mechanical problem and represents one of the very early successes of quantum mechanics [14], [20]. By noting that the interaction of a laser field is weak compared to the forces within the hydrogen atom, we can use perturbation theory to write the Hamiltonian for an unconstrained atomic particle interacting with a laser field as the sum of the free atomic Hamiltonian

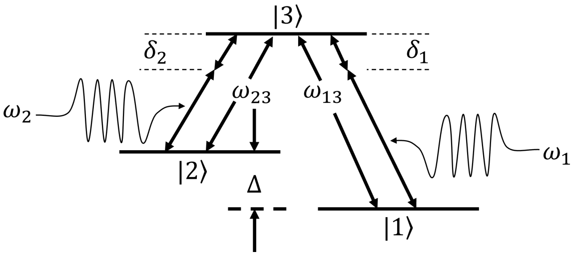

Figure 2.2. Lambda energy structure of ^{85}Rb. The frequencies, ω_{13} and ω_{23}, correspond to the resonant frequency of the energy transition from their respective quantum states. Ground state frequency splitting, $\Delta = \omega_{13} - \omega_{23}$, corresponds to the forbidden transition between states $|1\rangle \rightarrow |2\rangle$. Two separate lasers, operating at frequencies ω_1 and ω_2 respectively, apply an external electromagnetic field to the system where the laser detuning, δ_n, is defined by $\delta_n = \omega_{n3} - \omega_n$, and represents the distance off-resonance the laser is tuned.

(H_o) and an interaction Hamiltonian (H_I),

$$\hat{H}_{EIT} = H_o + H_I. \tag{2.5}$$

Of note, the caret identifier is used to indicate a quantum operator throughout this work. Also, we recognize the right to define an advantageous reference point and assign a zero-energy value to the state $|1\rangle$ and simplify the free atom Hamiltonian to

$$H_o = \hbar\Delta\,|2\rangle\,\langle 2| + \hbar\omega_{13}\,|3\rangle\,\langle 3| = \begin{bmatrix} 0 & 0 & 0 \\ 0 & \hbar\Delta & 0 \\ 0 & 0 & \hbar\omega_{13} \end{bmatrix}. \tag{2.6}$$

In writing (2.6), we first used standard quantum mechnaics bra-ket notation to write the Hamiltonian and then used standard linear algebra techniques to write the Hamiltonian in matrix notation. The interaction Hamiltonian, as the name suggests, is a function of the the atom-field interaction. When an atom interacts with the electromagnetic (EM) field, it undergoes a transition from its original state to a final state through a coupling with the transition dipole moment. It is defined by the dot product of the atomic dipole operator, $\hat{\mu}$, and the external EM field, where the dipole operator is given by

$$\hat{\mu} = \sum_{i=1}^{3}\sum_{j=1}^{3} |i\rangle \langle i| \mu |j\rangle \langle j| \,. \tag{2.7}$$

Here, we have used the quantum bra-ket notation, in which $|i\rangle$ represents the *ket* basis vector for the ith state and $\langle i|$ represents the corresponding *bra*. Our EM field is applied in the form of two coherent laser sources to drive the two atomic transitions, $|1\rangle \longrightarrow |3\rangle$ and $|2\rangle \longrightarrow |3\rangle$. We note that the interaction of the atom with the magnetic component of the laser field is a factor of c smaller than the interaction with the electric field, where c is the speed of light [21]. Therefore, it can be neglected in the interaction Hamiltonian equation,

$$H_I = -\hat{\mu} \cdot \vec{E} = -\vec{E} \cdot \begin{bmatrix} \vec{\mu}_{11} & \vec{\mu}_{12} & \vec{\mu}_{13} \\ \vec{\mu}_{21} & \vec{\mu}_{22} & \vec{\mu}_{23} \\ \vec{\mu}_{31} & \vec{\mu}_{32} & \vec{\mu}_{33} \end{bmatrix}, \tag{2.8}$$

where we have used the notation $\vec{\mu}_{ij} \equiv \langle i|\hat{\mu}|j\rangle$. To further simplify the interaction Hamiltonian, we recall that the transition from $|1\rangle \longrightarrow |2\rangle$ is dipole-forbidden, so that we can take $\vec{\mu}_{12} = \vec{\mu}_{21} = 0$. Likewise, we can write $\vec{\mu}_{ii} = 0$ by observing that a state cannot be coupled to itself via a dipole transition, which is a result of the dipole moment being an odd-parity operator. Finally, the interaction is simplified to

$$H_I = -\vec{E} \cdot \begin{bmatrix} 0 & 0 & \vec{\mu}_{13} \\ 0 & 0 & \vec{\mu}_{23} \\ \vec{\mu}_{31} & \vec{\mu}_{32} & 0 \end{bmatrix}. \tag{2.9}$$

Density Matrix

Schrödinger's Equation allows us to write a single atom's wave function as

$$\frac{\partial}{\partial t} |\psi\rangle = -\frac{i}{\hbar}\hat{H} |\psi\rangle \,. \tag{2.10}$$

However, the wave function is a single atom wave function that needs to be connected to the macroscopic response of the system. Therefore, to further our discussion we find an analog of Schrödinger's Equation in terms of the density operator and its time derivative below by writing

$$\hat{\rho} = \sum_n C_n \left|\psi_n\right\rangle \left\langle\psi_n\right| \tag{2.11}$$

and

$$\dot{\hat{\rho}} = \sum_n C_n \Big(\left|\dot{\psi}_n\right\rangle \left\langle\psi_n\right| + \left|\psi_n\right\rangle \left\langle\dot{\psi}_n\right| \Big), \tag{2.12}$$

where C_n are the coefficients that describe the superposition of wave functions. Substituting (2.10) into (2.12), we arrive at the von Neumann Equation,

$$\dot{\hat{\rho}} = -\frac{i}{\hbar}[H, \rho]. \tag{2.13}$$

This form of Schrödinger's Equation is advantageous because it does not restrict the evolution to pure states but rather generalizes the evolution to mixed states (e.g., when spontaneous emission is taken into account). We are now able to solve for the density matrix components that describe the change of population in each state and transitionally from one state to another. We use the notation $\rho_{ij} \equiv \langle i|\hat{\rho}|j\rangle$ to form the density matrix. A 3×3 matrix is formed for a three level system and by noting

$$\dot{\rho}_{ij} = \dot{\rho}^*_{ji} \tag{2.14}$$

the density operator takes the form

$$\dot{\hat{\rho}} = \begin{bmatrix} \dot{\rho}_{11} & \dot{\rho}_{12} & \dot{\rho}_{13} \\ \dot{\rho}^*_{12} & \dot{\rho}_{22} & \dot{\rho}_{23} \\ \dot{\rho}^*_{13} & \dot{\rho}^*_{23} & \dot{\rho}_{33} \end{bmatrix}. \tag{2.15}$$

Using (2.13), we can derive coupled equations for each density matrix element:

$$\dot{\rho}_{12} = i\Delta\rho_{12} + \frac{i}{\hbar}(\vec{\mu}_{13}\rho_{32} - \vec{\mu}_{23}^{*}\rho_{13}) \cdot \vec{E}, \tag{2.16a}$$

$$\dot{\rho}_{13} = i\omega_{13}\rho_{13} + \frac{i}{\hbar}(\vec{\mu}_{13}(\rho_{33} - \rho_{11}) - \vec{\mu}_{23}\rho_{12}) \cdot \vec{E}, \tag{2.16b}$$

$$\dot{\rho}_{22} = \frac{i}{\hbar}(\vec{\mu}_{23}\rho_{32} - \vec{\mu}_{23}^{*}\rho_{23}) \cdot \vec{E}, \tag{2.16c}$$

$$\dot{\rho}_{23} = i(\omega_{13} - \Delta)\rho_{23} + \frac{i}{\hbar}(\vec{\mu}_{23}(\rho_{33} - \rho_{22}) - \vec{\mu}_{13}\rho_{21}) \cdot \vec{E}, \tag{2.16d}$$

$$\dot{\rho}_{33} = \frac{i}{\hbar}(\vec{\mu}_{13}^{*}\rho_{13} + \vec{\mu}_{23}^{*}\rho_{23} - \vec{\mu}_{13}\rho_{31} - \vec{\mu}_{23}\rho_{32}) \cdot \vec{E}. \tag{2.16e}$$

Now, let us consider the electric field, $\vec{E}$, which is defined in a classical vector-field manner. From Figure 2.2, we recognize two fields are required to drive the two atomic transitions. The probe and pump fields will drive the $|1\rangle \rightarrow |3\rangle$ and $|2\rangle \rightarrow |3\rangle$ transitions, respectively. The total electric field is given by

$$\vec{E} = \vec{E}_1 + \vec{E}_2, \tag{2.17}$$

where

$$\vec{E}_1 = \vec{\varepsilon}_1 e^{-i(\omega_1 t - k_1 z)} + (c.c.), \tag{2.18a}$$

$$\vec{E}_2 = \vec{\varepsilon}_2 e^{-i(\omega_2 t - k_2 z)} + (c.c.). \tag{2.18b}$$

Here, $\vec{\varepsilon}_i$ is the product of the field amplitude and polarization vector, ω_i is the angular frequency, and k_i is the associated k-vector for the ith field (with $i = 1, 2$). With some foresight, a direct substitution of (2.17) into (2.16a)–(2.16e) will result in many complex exponential terms. In order to remove dependence on time and terms oscillating at very high frequencies, it is advantageous to apply a judicious change of basis followed by making the rotating wave approximation (RWA) in which the counter-rotating terms that oscillate at twice the optical frequencies are ignored since they make negligible contributions to the dynamics

$$\rho_{ii} = \tilde{\rho}_{ii}, \tag{2.19a}$$

$$\rho_{ij} = \tilde{\rho}_{ij} e^{i(\omega_L t - k_L z)}, \tag{2.19b}$$

where the tilde denotes the density operator in the transformed basis and where the following cases apply:

$$ij = \begin{cases} 12,\ \omega_L = \Delta \text{ and } k_L = (k_1 - k_2), \\ 13,\ \omega_L = \omega_1 \text{ and } k_L = k_1, \\ 23,\ \omega_L = \omega_2 \text{ and } k_L = k_2. \end{cases} \tag{2.20}$$

The transformation allows (2.16a)–(2.16e) to be conveniently simplified into the following form:

$$\dot{\tilde{\rho}}_{12} = i\tilde{\rho}_{12}(\Delta - (\omega_1 - \omega_2) + (k_1 - k_2)v) + \frac{i}{\hbar}(\vec{\mu}_{13} \cdot \vec{\varepsilon}_1^{\,*} \tilde{\rho}_{32} - \vec{\mu}_{23}^{\,*} \cdot \vec{\varepsilon}_2 \tilde{\rho}_{13}), \tag{2.21a}$$

$$\dot{\tilde{\rho}}_{13} = i\tilde{\rho}_{13}(\omega_{13} - \omega_1 + k_1 v) + \frac{i}{\hbar}(\vec{\mu}_{13} \cdot \vec{\varepsilon}_1^{\,*}(\tilde{\rho}_{33} - \tilde{\rho}_{11}) - \vec{\mu}_{23} \cdot \vec{\varepsilon}_2^{\,*} \tilde{\rho}_{12}), \tag{2.21b}$$

$$\dot{\tilde{\rho}}_{22} = \frac{i}{\hbar}(\vec{\mu}_{23} \cdot \vec{\varepsilon}_2^{\,*} \tilde{\rho}_{32} - \vec{\mu}_{23}^{\,*} \cdot \vec{\varepsilon}_2 \tilde{\rho}_{23}), \tag{2.21c}$$

$$\dot{\tilde{\rho}}_{23} = i\tilde{\rho}_{23}(\omega_{23} - \omega_2 + k_2 v) + \frac{i}{\hbar}(\vec{\mu}_{23} \cdot \vec{\varepsilon}_2^{\,*}(\tilde{\rho}_{33} - \tilde{\rho}_{22}) - \vec{\mu}_{13} \cdot \vec{\varepsilon}_1^{\,*} \tilde{\rho}_{21}), \tag{2.21d}$$

$$\dot{\tilde{\rho}}_{33} = \frac{i}{\hbar}(\vec{\mu}_{13}^{\,*} \cdot \vec{\varepsilon}_1 \tilde{\rho}_{13} + \vec{\mu}_{23}^{\,*} \cdot \vec{\varepsilon}_2 \tilde{\rho}_{23} - \vec{\mu}_{13} \cdot \vec{\varepsilon}_1^{\,*} \tilde{\rho}_{31} - \vec{\mu}_{23} \cdot \vec{\varepsilon}_2^{\,*} \tilde{\rho}_{32}). \tag{2.21e}$$

We further identify laser detuning as the difference between the laser frequency and the frequency of the respective atomic transition

$$\delta_1 = \omega_1 - \omega_{13}, \tag{2.22}$$

$$\delta_2 = \omega_2 - \omega_{23}, \tag{2.23}$$

$$\delta_2 - \delta_1 = \Delta - (\omega_1 - \omega_2), \tag{2.24}$$

where δ_1 and δ_2 represent the single-photon detuning of each laser from its respective transition, and $\delta_2 - \delta_1$ is the two-photon detuning of the combined laser fields from the ground state transition frequency. It is also convenient to describe these equations in terms of the Rabi frequency, which quantifies the frequency at which the system oscillates between its energy levels due to the applied fields. The Rabi frequencies of the two transitions are given as

$$\Omega_1 = \frac{2\vec{\mu}_{13}^{*} \cdot \vec{\varepsilon}_1}{\hbar}, \tag{2.25}$$

$$\Omega_2 = \frac{2\vec{\mu}_{23}^{*} \cdot \vec{\varepsilon}_2}{\hbar}, \tag{2.26}$$

and thus (2.21a)–(2.21e) become

$$\dot{\tilde{\rho}}_{12} = i\tilde{\rho}_{12}((\delta_2 - \delta_1) + (k_1 - k_2)v) + \frac{i}{2}(\Omega_1^{*}\tilde{\rho}_{32} - \Omega_2\tilde{\rho}_{13}), \tag{2.27a}$$

$$\dot{\tilde{\rho}}_{13} = i\tilde{\rho}_{13}(k_1 v - \delta_1) + \frac{i}{2}(\Omega_1^{*}(\tilde{\rho}_{33} - \tilde{\rho}_{11}) - \Omega_2^{*}\tilde{\rho}_{12}), \tag{2.27b}$$

$$\dot{\tilde{\rho}}_{22} = \frac{i}{2}(\Omega_2^{*}\tilde{\rho}_{32} - \Omega_2\tilde{\rho}_{23}), \tag{2.27c}$$

$$\dot{\tilde{\rho}}_{23} = i(k_2 v - \delta_2)\tilde{\rho}_{23} + \frac{i}{2}(\Omega_2^{*}(\tilde{\rho}_{33} - \tilde{\rho}_{22}) - \Omega_1^{*}\tilde{\rho}_{21}), \tag{2.27d}$$

$$\dot{\tilde{\rho}}_{33} = \frac{i}{2}(\Omega_1\tilde{\rho}_{13} + \Omega_2\tilde{\rho}_{23} - \Omega_1^{*}\tilde{\rho}_{31} - \Omega_2^{*}\tilde{\rho}_{32}). \tag{2.27e}$$

Finally, we consider incoherent decay and recognize that the system experiences spontaneous decay from the excited state that is not yet captured in our semi-classical approach. A method to properly include these effects is presented in [19], by adding the following phenomenological decay terms,

$$\dot{\tilde{\rho}}_{ij} = -\gamma_{ij}\tilde{\rho}_{ij}, \tag{2.28a}$$

$$\dot{\tilde{\rho}}_{22} = W_{32}\tilde{\rho}_{33} + W_{12}\tilde{\rho}_{11} - W_{21}\tilde{\rho}_{22}, \tag{2.28b}$$

$$\dot{\tilde{\rho}}_{33} = -(W_{32} + W_{31})\tilde{\rho}_{33}, \tag{2.28c}$$

where W_{ij} is the decay from level i to j and upward transitions are assumed to be zero. Likewise, γ_{ij} is the polarization decay rate for the $i \longrightarrow j$ transition and given by

$$\gamma_{ij} = \frac{1}{2}\sum_{k=1}^{3}(W_{ik} + W_{jk}). \tag{2.29}$$

Finally, we use the fact that we are considering a closed system, subject to the constraint $\tilde{\rho}_{11} + \tilde{\rho}_{22} + \tilde{\rho}_{33} = 1$ must be satisfied (which represents the physical constraint that the population must be in one of the three states or equivalently the population probability must add to one). Therefore, we arrive at the following equations:

$$\dot{\tilde{\rho}}_{12} = i\tilde{\rho}_{12}((\delta_2 - \delta_1) + (k_1 - k_2)v) + \frac{i}{2}(\Omega_1^*\tilde{\rho}_{32} - \Omega_2\tilde{\rho}_{13}) - \gamma_{12}\tilde{\rho}_{12}, \tag{2.30a}$$

$$\dot{\tilde{\rho}}_{13} = i\tilde{\rho}_{13}(k_1 v - \delta_1) + \frac{i}{2}(\Omega_1^*(\tilde{\rho}_{33} - \tilde{\rho}_{11}) - \Omega_2^*\tilde{\rho}_{12}) - \gamma_{13}\tilde{\rho}_{13}, \tag{2.30b}$$

$$\dot{\tilde{\rho}}_{22} = \frac{i}{2}(\Omega_2^*\tilde{\rho}_{32} - \Omega_2\tilde{\rho}_{23}) + (W_{32}\tilde{\rho}_{33} - W_{21}\tilde{\rho}_{22}), \tag{2.30c}$$

$$\dot{\tilde{\rho}}_{23} = i(k_2 v - \delta_2)\tilde{\rho}_{23} + \frac{i}{2}(\Omega_2^*(\tilde{\rho}_{33} - \tilde{\rho}_{22}) - \Omega_1^*\tilde{\rho}_{21}) - \gamma_{23}\tilde{\rho}_{23}, \tag{2.30d}$$

$$\dot{\tilde{\rho}}_{33} = \frac{i}{2}(\Omega_1\tilde{\rho}_{13} + \Omega_2\tilde{\rho}_{23} - \Omega_1^*\tilde{\rho}_{31} - \Omega_2^*\tilde{\rho}_{32}) - (W_{32} + W_{31})\tilde{\rho}_{33}. \tag{2.30e}$$

We can focus on the three transition densities that describe how the system transitions between states: $\dot{\tilde{\rho}}_{12}, \dot{\tilde{\rho}}_{13}$, and $\dot{\tilde{\rho}}_{23}$. To model the experiment, we consider the conditions for EIT in which the probe field is much weaker than the pump field (i.e., $\Omega_2 >> \Omega_1$). In this case, second order terms of the probe field, Ω_1^2, can be dropped as they will be dominated by the remaining first order terms. Additionally, we find that $\tilde{\rho}_{23}$ is first order in terms of the probe field; therefore, the expression $\frac{i}{2}\Omega_1^*\tilde{\rho}_{32}$ can be neglected by the same logic, producing the coupled equations

$$\dot{\tilde{\rho}}_{12} = -[\gamma_{12} - i((\delta_2 - \delta_1) - (k_2 - k_1)v)]\tilde{\rho}_{12} - \frac{i}{2}\Omega_2\tilde{\rho}_{13}, \tag{2.31a}$$

$$\dot{\tilde{\rho}}_{13} = -\frac{i}{2}\Omega_2^*\tilde{\rho}_{12} - [\gamma_{13} + i(\delta_1 - k_1 v)]\tilde{\rho}_{13} - \frac{i}{2}\Omega_1^*. \tag{2.31b}$$

Solving in steady state, we have

$$\tilde{\rho}_{12} = \frac{\Omega_1^*\Omega_2}{4[\gamma_{12} - i((\delta_2 - \delta_1) - (k_2 - k_1)v)][\gamma_{13} + i(\delta_1 - k_1 v)] + \Omega_2^2}, \tag{2.32a}$$

$$\tilde{\rho}_{13} = -\frac{i[\gamma_{12} - i((\delta_2 - \delta_1) - (k_2 - k_1)v)]\Omega_1^*}{2[\gamma_{12} - i((\delta_2 - \delta_1) - (k_2 - k_1)v)][\gamma_{13} + i(\delta_1 - k_1 v)] + \Omega_2^2}. \tag{2.32b}$$

These equations illuminate a controllable scheme to drive quantum state transition within the 3-level ^{85}Rb system and align with similar work published by [18], [22]. In the follow-on section, we explore the relationship between population density and linear susceptibility of the storage medium.

Population Density to Susceptibility

To show how linear susceptibility of a medium is dependent on the population density, we consider the wave equation for the full Maxwell field [22],

$$\Big(\frac{\partial^2}{\partial \mathrm{t}^2} - \mathrm{c}^2\frac{\partial^2}{\partial \mathrm{z}^2}\Big)\bar{E} = -\frac{1}{\epsilon_o}\frac{\partial^2}{\partial \mathrm{t}^2}\mathcal{P}, \tag{2.33}$$

where $\mathcal{P}$ is the macroscopic polarization defined by the dipole moment per unit volume [18]. If we let $\mathcal{N}$ be the atomic density, we can express the macroscopic polarization in terms of the microscopic polarization by

$$\begin{aligned}\mathcal{P} &= \mathcal{N}\langle\hat{\mu}\rangle,\\ &= \mathcal{N}[\mu_{13}\tilde{\rho}_{31}e^{-i(\omega_1 t - k_1 z)} + \text{c.c.} + \mu_{23}\tilde{\rho}_{32}e^{-i(\omega_2 t - k_2 z)} + \text{c.c.}],\end{aligned} \tag{2.34}$$

where we have used the fact that $\langle\hat{\mu}\rangle = \mathbf{Tr}[\rho\hat{\mu}]$ where **Tr** denotes the trace over the atomic basis vectors. Starting with the left-hand side of (2.33), we distribute the electric field term

$$\Big(\ddot{E} - \mathrm{c}^2\frac{\partial^2}{\partial \mathrm{z}^2}E\Big), \tag{2.35}$$

where,

$$\ddot{E} = (-\omega_1^2\varepsilon_1 - i2\omega_1\dot{\varepsilon_1} + \ddot{\varepsilon_1})e^{-i(\omega_1 t-k_1 z)} + (-\omega_2^2\varepsilon_2 - i2\omega_2\dot{\varepsilon_2} + \ddot{\varepsilon_2})e^{-i(\omega_2 t-k_2 z)} + \text{c.c.}, \tag{2.36}$$

and,

$$\begin{aligned}\frac{\partial^2}{\partial z^2}E = (-k_1^2\varepsilon_1 + i2k_1\frac{\partial\varepsilon_1}{\partial z} + \frac{\partial^2\varepsilon_1}{\partial z^2})e^{-i(\omega_1 t-k_1 z)} \\ + (-k_2^2\varepsilon_2 + i2k_2\frac{\partial\varepsilon_2}{\partial z} + \frac{\partial^2\varepsilon_2}{\partial z^2})e^{-i(\omega_2 t-k_2 z)} + \text{c.c.}\end{aligned} \tag{2.37}$$

Similarly, the right-hand side of (2.33) is found to be

$$\ddot{\mathcal{P}} = \mathcal{N}\Big(\mu_{13}(-\omega_1^2\tilde{\rho}_{31} - i2\omega_1\dot{\tilde{\rho}}_{31} + \ddot{\tilde{\rho}}_{31})e^{-i(\omega_1 t-k_1 z)} + \mu_{23}(-\omega_2^2\tilde{\rho}_{32} - i2\omega_2\dot{\tilde{\rho}}_{32} + \ddot{\tilde{\rho}}_{32})e^{-i(\omega_2 t-k_2 z)} + \text{c.c.}\Big). \tag{2.38}$$

Equating the left and right-hand sides, the resulting second order differential equation becomes very complex. So, we consider a reduced wave equation in which a slowly varying envelop assumption allows us to consider the second-order terms negligible, and we arrive at

$$\begin{aligned}&(-\omega_1^2\varepsilon_1 - i2\omega_1\dot{\varepsilon_1})e^{-i(\omega_1 t-k_1 z)} + (-\omega_2^2\varepsilon_2 - i2\omega_2\dot{\varepsilon_2})e^{-i(\omega_2 t-k_2 z)} \\ &\quad - c^2\Big((-k_1^2\varepsilon_1 + i2k_1\frac{\partial\varepsilon_1}{\partial z})e^{-i(\omega_1 t-k_1 z)} + (-k_2^2\varepsilon_2 + i2k_2\frac{\partial\varepsilon_2}{\partial z})e^{-i(\omega_2 t-k_2 z)}\Big) \\ &= \\ &\quad -\frac{\mathcal{N}}{\epsilon_o}\Big(\mu_{13}(-\omega_1^2\tilde{\rho}_{31} - i2\omega_1\dot{\tilde{\rho}}_{31})e^{-i(\omega_1 t-k_1 z)} + \mu_{23}(-\omega_2^2\tilde{\rho}_{32} - i2\omega_2\dot{\tilde{\rho}}_{32})e^{-i(\omega_2 t-k_2 z)}\Big).\end{aligned} \tag{2.39}$$

However, further simplification is accomplished by recognizing the dominant terms ($\omega^2\tilde{\rho}_{3i} >> 2\omega\dot{\tilde{\rho}}_{3i}$, $i = 1, 2$) and matching the resulting time-dependent exponential terms, which is also a result of the slowly varying wave approximation. The resulting wave equation has two components corresponding to the two applied laser fields. Their respective definitions are

$$\begin{aligned}
(-\omega_1^2\varepsilon_1 - i2\omega_1\dot{\varepsilon}_1) - c^2(-k_1^2\varepsilon_1 + i2k_1\frac{\partial\varepsilon_1}{\partial \mathrm{z}}) &= -\frac{\mu_{13}\mathcal{N}}{\epsilon_o}(-\omega_1^2\tilde{\rho}_{31}),\\
-i2\omega_1\dot{\varepsilon}_1 - i2c\omega_1\frac{\partial\varepsilon_1}{\partial \mathrm{z}} &= -\frac{\mu_{13}\mathcal{N}}{\epsilon_o}(-\omega_1^2\tilde{\rho}_{31}),\\
\dot{\varepsilon}_1 + c\frac{\partial\varepsilon_1}{\partial \mathrm{z}} &= \frac{i\mu_{13}\mathcal{N}\omega_1}{2\epsilon_o}\tilde{\rho}_{31}, \qquad (2.40a)\\
(-\omega_2^2\varepsilon_2 - i2\omega_2\dot{\varepsilon}_2) - c^2(-k_2^2\varepsilon_2 + i2k_2\frac{\partial\varepsilon_2}{\partial \mathrm{z}}) &= \frac{\mu_{23}\mathcal{N}}{\epsilon_o}(-\omega_2^2\tilde{\rho}_{32}),\\
-i2\omega_2\dot{\varepsilon}_2 - i2c\omega_2\frac{\partial\varepsilon_2}{\partial \mathrm{z}} &= \frac{\mu_{23}\mathcal{N}}{\epsilon_o}(-\omega_2^2\tilde{\rho}_{32}),\\
\dot{\varepsilon}_2 + c\frac{\partial\varepsilon_2}{\partial \mathrm{z}} &= \frac{i\mu_{23}\mathcal{N}\omega_2}{2\epsilon_o}\tilde{\rho}_{32}. \qquad (2.40b)
\end{aligned}$$

For a continuous wave, the time-derivative of the field is zero in (2.40a) and (2.40b). Having derived an equation for the probe field amplitude ε_1, we can now convert the equation into one involving the local Rabi frequency using (2.25),

$$\frac{d}{dz}\Omega_1 = i\alpha W_{31}\tilde{\rho}_{31}, \qquad (2.41)$$

where α is the absorption length scaled by the decay rate, W_{31},

$$\alpha = \frac{\omega_1|\mu_{13}|^2\mathcal{N}}{\hbar\epsilon_o c W_{31}}. \qquad (2.42)$$

By inspection, (2.41) can be massaged into a common form of Beer's Law,

$$\begin{aligned}
\frac{d\Omega_1}{dz} &= i\alpha W_{31}\Big(\frac{[\gamma_{12} + i((\delta_2 - \delta_1) - (k_2 - k_1)v)]\Omega_1}{-2i[\gamma_{12} + i((\delta_2 - \delta_1) - (k_2 - k_1)v)][\gamma_{13} - i(\delta_1 - k_1 v)] - i\Omega_2^2}\Big),\\
\frac{d\Omega_1}{\Omega_1} &= \alpha W_{31}\frac{i\gamma_{13} - (\delta_1 - k_1 v)}{2[\gamma_{13}^2 + (\delta_1 - k_1 v)^2] + \Omega_2^2\Big(\frac{[\gamma_{13}+i(\delta_1-k_1v)]}{[\gamma_{12}+i((\delta_2-\delta_1)-(k_2-k_1)v)]}\Big)}dz. \qquad (2.43)
\end{aligned}$$

We make the substitution,

$$\chi = \alpha W_{31} \frac{i\gamma_{13} - (\delta_1 - k_1 v)}{2[\gamma_{13}^2 + (\delta_1 - k_1 v)^2] + \Omega_2^2 \left(\frac{[\gamma_{13} + i(\delta_1 - k_1 v)]}{[\gamma_{12} + i((\delta_2 - \delta_1) - (k_2 - k_1) v)]} \right)}, \tag{2.44}$$

into Eq. (2.43), such that,

$$\frac{d\Omega_1}{\Omega_1} = \chi dz, \tag{2.45}$$

and integrate both sides, to solve for the spatially dependent Rabi frequency of the probe beam. A modulus square relationship exists between the Rabi frequency and field intensity by

$$\begin{aligned} I(z) &= |\Omega_1(z)|^2, \\ &= |\Omega_1(0)|^2 e^{2\chi z}. \end{aligned} \tag{2.46}$$

Known as linear susceptibility, χ describes the dissipation response, or absorption, and refractive index, n, of the medium through its real and imaginary components, respectively. Here, the controllable term is Ω_2^2, which is proportional to the strength of the pump beam and will be an important factor when considering *slow light*. Also, the forbidden transition of an ideal EIT medium between two ground states implies the decoherence term, γ_{12}, is very small ($\Omega_2 >> \gamma_{12}$). The susceptibility can be broken down into real and imaginary parts,

$$\chi = \mathrm{Re}(\chi) + i\mathrm{Im}(\chi), \tag{2.47}$$

where if we assume an ideal EIT medium ($\gamma_{12} \rightarrow 0$) and the pump is weak with respect to the excited state polarization decay rate ($\Omega_2 << \gamma_{13}$),

$$\mathrm{Re}(\chi) = -\alpha W_{31} \frac{\delta_1 - k_1 v}{[\gamma_{13}^2 + (\delta_1 - k_1 v)^2]}, \tag{2.48a}$$

$$\mathrm{Im}(\chi) = \alpha W_{31} \frac{\gamma_{13}}{[\gamma_{13}^2 + (\delta_1 - k_1 v)^2]}, \tag{2.48b}$$

A plot of (2.48b) produces the natural Lorentzian curve, which describes absorption when the probe beam is scanned over resonance. Similarly, (2.48a) converges to zero as the probe beam approaches resonance indicating phase and group velocity of the beam is equal to that of light in a vacuum by the relationships

$$n = 1 + \frac{1}{2}\mathrm{Re}(\chi), \tag{2.49}$$

$$v_p = \frac{c}{n}, \tag{2.50}$$

and

$$v_g = \frac{c}{n + \omega\frac{\partial n}{\partial \omega}}. \tag{2.51}$$

Phase and group velocity of a beam are the speeds at which the individual carrier waves and the envelope of the wave packet propagate in time, respectively. Group velocity is often the more appropriate term when describing the speed of information bearing waveforms. Then, by simple substitution, we see that the group velocity of the probe beam is controllable and behaves like

$$v_g = \frac{c}{1 + \frac{\alpha W_{31}}{\Omega_2^2}}. \tag{2.52}$$

These equations support conclusions found in [11] and [18]. Indeed, under appropriate conditions, these equations indicate that group velocities as low as $c/10^6$ to $c/10^7$ can be achieved [11]. These findings have spurred a great deal of research in the realm of non-linear optics and have been critical in the exploration of the optical phenomenon slow light. In the following section we consider these procedures through the lens of communication systems and explore how a pulse behaves under the conditions of slow light.

2.2 EIT Response of a Gaussian Pulse

As previously mentioned, this derivation is motivated through the lens of information systems where data are often transferred on a carrier signal consisting of many pulses. To begin, we redefine the probe field to take into account the fact that the field is now a pulse in time:

$$\begin{aligned} \varepsilon_1(z,t) &= \int_{-\infty}^{\infty} A(z,\omega) e^{i\omega t}\, d\omega, \\ \varepsilon_1(z,t) &= \int_{-\infty}^{\infty} A(z,\delta) e^{i(\omega_1+\delta)t}\, d\delta. \end{aligned} \tag{2.53}$$

where $A(z,\delta)$ is the Fourier transform of the electric field pulse envelope and δ is the frequency difference from the carrier frequency. We can directly substitute (2.53) into (2.40a) to arrive at

$$\int_{-\infty}^{\infty} \left(i\delta A + c\frac{\partial A}{\partial \mathrm{z}} \right) e^{i\delta t}\, d\delta = \frac{i\mu_{13}\mathcal{N}\omega_1}{2\epsilon_o}\tilde{\rho}_{31}. \tag{2.54}$$

In a similar manner, $\tilde{\rho}_{31}$ represents the atomic response to a field; therefore if the field is pulsed, it makes sense that the response of the medium as captured by $\tilde{\rho}_{31}$ is also pulsed. Thus, we can write

$$\tilde{\rho}_{31} = \int_{-\infty}^{\infty} B(z,\delta) e^{i\delta t}\, d\delta, \tag{2.55}$$

where $B(z,\delta)$ is the Fourier transform of $\tilde{\rho}_{31}$ and where we note that the carrier frequency was already removed when we transformed ρ to $\tilde{\rho}$. Equation (2.54) can be written as

$$\int_{-\infty}^{\infty} \left(i\delta A + c\frac{\partial A}{\partial \mathrm{z}} \right) e^{i\delta t}\, d\delta = \frac{i\mu_{13}\mathcal{N}\omega_1}{2\epsilon_o} \int_{-\infty}^{\infty} B(z,\delta) e^{i\delta t}\, d\delta. \tag{2.56}$$

We see that both sides integrate over the same range and integration variable; therefore, we are allowed to equate the integrands, solve the equation for each detuning term individually, and sum the solutions to arrive at the atomic response to a pulsed field. The general solution to this equation follows as such:

$$\frac{\partial A}{\partial \mathrm{z}} = -i\frac{\delta}{c}A + i\frac{\mu_{13}\mathcal{N}\omega_1}{2c\epsilon_o}B, \tag{2.57a}$$

$$\frac{\partial \Omega_1}{\partial \mathrm{z}} = -i\frac{\delta}{c}\Omega_1 + \frac{|\mu_{13}|^2\mathcal{N}\omega_1}{\hbar\epsilon_o c}\Omega_1 B^*, \tag{2.57b}$$

$$\frac{\partial \Omega_1}{\Omega_1} = -i\frac{\delta}{c} + \alpha W_{31} B^* dz, \tag{2.57c}$$

where we make the substitution for $A(z, \delta)$ from the relationship in (2.25) and condense the final expression with

$$\chi = -i\frac{\delta}{c} + \alpha W_{31} B^*, \tag{2.58}$$

$$B^* = \frac{i\gamma_{13} - (\delta - k_\delta v)}{2[\gamma_{13}^2 + (\delta - k_\delta v)^2] + \Omega_2^2 \left(\frac{[\gamma_{13} + i(\delta - k_\delta v)]}{[\gamma_{12} + i((\delta_2 - \delta) - (k_2 - k_\delta)v)]} \right)}. \tag{2.59}$$

We relate field intensity to local Rabi frequency as

$$\begin{aligned} I(z, \delta) &= \int_{-\infty}^{\infty} |A(z, \delta)|^2 \, d\delta, \\ &= \int_{-\infty}^{\infty} |A_o(0, \delta)|^2 e^{2\chi z} \, d\delta. \end{aligned} \tag{2.60}$$

Applying the constraints of an ideal EIT medium and weak pump beam, linear susceptibility appears similar to (2.48b) but with an additional non-zero term in the absorption response that depends on the detuning factor:

$$\mathrm{Re}(\chi) = -2\alpha W_{31} \int_{-\infty}^{\infty} \frac{(\delta - k_\delta v)}{[\gamma_{13}^2 + (\delta - k_\delta v)^2]} \, d\delta, \tag{2.61}$$

$$\mathrm{Im}(\chi) = 2 \int_{-\infty}^{\infty} \left(-\frac{\delta}{c} + \alpha W_{31} \frac{\gamma_{13}}{[\gamma_{13}^2 + (\delta - k_\delta v)^2]} \right) d\delta. \tag{2.62}$$

We interpret these results in the following way. We have derived an expression for the susceptibility of a continuous probe field. For pulses with sufficiently slow amplitude variations, we can decompose the pulse into individual frequency components, solve for the susceptibility as we did for the continuous field but with an added detuning, and then sum the results together with the same decomposition weighting. In regards to slow light, we find a similar conclusion in comparison to the case of a continuous wave. Group velocity of the probe beam is expected to be slow in the same manner and behave in a similar fashion to (2.52).

2.3 EIT Response of a Gaussian Pulse with Amplitude Modulation

Finally, we seek to apply modulation to the pulsed probe. This is very similar to the previous section except for the addition of a generalized time-varying amplitude term, which arises from taking the Fourier transform of a modulated pulse instead of a simple pulse. We start by modifying the probe field with a time-varying function, $m(t)$, and computing the Fourier transform of the convolved frequency responses:

$$\varepsilon(z,t) = m(t)a(z,t), \tag{2.63}$$

$$\varepsilon(z,t) = \int_{-\infty}^{\infty} \Big(M(\omega) * A(z,\omega)\Big) e^{i\omega t}\, d\omega. \tag{2.64}$$

We define our time-varying function, $m(t)$, as the even function

$$m(t) = \cos^2(\omega_m t), \tag{2.65}$$

which assumes the frequency response

$$M(\omega) = \delta(\omega) + \frac{1}{2}\Big(\delta(\omega - 2\omega_m) + \delta(\omega + 2\omega_m)\Big). \tag{2.66}$$

The computation of the convolution from (2.64) is then

$$\varepsilon(z,t) = \int_{-\infty}^{\infty} \Big[A(z,\omega) + \frac{1}{2}\Big(A(z,\omega - 2\omega_m) + A(z,\omega + 2\omega_m)\Big)\Big] e^{i\omega t}\, d\omega, \tag{2.67}$$

and can be written in terms of δ as

$$\varepsilon(z,t) = \int_{-\infty}^{\infty} \Big[A(z,\delta) + \frac{1}{2}\Big(A(z,\delta - 2\delta_m) + A(z,\delta + 2\delta_m)\Big)\Big] e^{i\delta t}\, d\delta. \tag{2.68}$$

To condense further derivations, we will refer to the integrand in (2.68) as A'. Applied to (2.40a), we have

$$\int_{-\infty}^{\infty} \Big(-i\delta A' + c\frac{\partial}{\partial \mathrm{z}} A' \Big) e^{i\delta t}\, d\delta = -\frac{i\mu_{13}\mathcal{N}\omega_1}{\epsilon_o}\tilde{\rho}_{31}. \tag{2.69}$$

As in the previous section, $\tilde{\rho}_{31}$ is considered to have a pulse-like response,

$$\tilde{\rho}_{31} = \int_{-\infty}^{\infty} \Big[B(z,\delta) + \frac{1}{2}\Big(B(z,\delta - 2\delta_m) + B(z,\delta + 2\delta_m) \Big) \Big] e^{i\delta t}\, d\delta, \tag{2.70}$$

where we note B' will, likewise, refer to the integrand and that the carrier frequency was already removed when we transformed ρ to $\tilde{\rho}$. Inspecting the equations, we expect three response peaks that arise from our follow-on derivations. They will include the normal response peak around resonance, with two shifted peaks on either side by a factor of $2\delta_m$. Our Beers Law equations are then

$$\frac{\partial A'}{\partial \mathrm{z}} = -i\frac{\delta}{c}A' + i\frac{\mu_{13}\mathcal{N}\omega_1}{c\epsilon_o}B', \tag{2.71a}$$

$$\frac{\partial \Omega_1}{\partial \mathrm{z}} = -i\frac{\delta}{c}\Omega_1 + \alpha W_{31}\Omega_1 B^*, \tag{2.71b}$$

$$\frac{\partial \Omega_1}{\Omega_1} = -i\frac{\delta}{c} + \alpha W_{31} B^* dz, \tag{2.71c}$$

where we make the substitution for $A'(z,\delta)$ from the relationship in (2.25) and condense the final expression with

$$\chi = -i\frac{\delta}{c} + \alpha W_{31}B^*, \tag{2.72}$$

$$B^* = \sum_{i=1}^{3} \frac{i\gamma_{13} - (\delta_i - k_\delta v)}{2[\gamma_{13}^2 + (\delta_i - k_\delta v)^2] + \Omega_2^2\Big(\frac{[\gamma_{13}+i(\delta_i - k_\delta v)]}{[\gamma_{12}+i((\delta_2-\delta_i)-(k_2-k_\delta)v)]}\Big)}, \tag{2.73}$$

where, in each case above,

$$i = \begin{cases} 1, \ \delta_1 = \delta, \\ 2, \ \delta_2 = \delta - 2\delta_m + k_m v, \\ 3, \ \delta_3 = \delta + 2\delta_m - k_m v. \end{cases} \tag{2.74}$$

From here, we determine field intensity as

$$\begin{aligned} I(z,\delta) &= \int_{-\infty}^{\infty} |A'(z,\delta)|^2 \, d\delta, \\ &= \int_{-\infty}^{\infty} |A'_o(0,\delta)|^2 e^{2\chi z} \, d\delta. \end{aligned} \tag{2.75}$$

Extracting the real and imaginary components of linear susceptibility under ideal EIT medium and weak pump conditions provide

$$\begin{aligned} \mathsf{Re}(\chi) = -2\alpha W_{31} \int_{-\infty}^{\infty} \Big[& \frac{(\delta - k_\delta v)}{[\gamma_{13}^2 + (\delta - k_\delta v)^2]} + \\ & \frac{1}{2} \frac{(\delta - 2\delta_m + 2k_m v - k_\delta v)}{[\gamma_{13}^2 + (\delta - 2\delta_m + 2k_m v - k_\delta v)^2]} + \\ & \frac{1}{2} \frac{(\delta + 2\delta_m - 2k_m v - k_\delta v)}{[\gamma_{13}^2 + (\delta + 2\delta_m - 2k_m v - k_\delta v)^2]} \Big] \, d\delta, \end{aligned} \tag{2.76a}$$

$$\begin{aligned} \mathsf{Im}(\chi) = 2 \int_{-\infty}^{\infty} \Big[& \frac{\delta}{c} + \alpha W_{31} \frac{\gamma_{13}}{[\gamma_{13}^2 + (\delta - k_\delta v)^2]} + \\ & \frac{\delta - 2\delta_m}{c} + \alpha W_{31} \frac{1}{2} \frac{\gamma_{13}}{[\gamma_{13}^2 + (\delta - 2\delta_m + 2k_m v - k_\delta v)^2]} + \\ & \frac{\delta + 2\delta_m}{c} + \alpha W_{31} \frac{1}{2} \frac{\gamma_{13}}{[\gamma_{13}^2 + (\delta + 2\delta_m - 2k_m v - k_\delta v)^2]} \Big] \, d\delta. \end{aligned} \tag{2.76b}$$

Thus, we infer from (2.76a) that the change in index of refraction vs. detuning produces three spectral regions where $\frac{\partial n}{\partial \omega}$ is very large. With appropriate selection of the modulation scheme such that its bandwidth does not exceed the transparency window, the underlying Gaussian pulse and the applied modulation can be delayed. However, inspection of (2.76b) indicates that more absorption-related signal distortion is likely, which aligns with conclusions made through explicit experimentation by [23]. In the following chapter, we will describe the table-top experiment used to test these theories.

THIS PAGE INTENTIONALLY LEFT BLANK

CHAPTER 3:
Experimental Apparatus

In this chapter we will review the experimental apparatus and examine techniques and procedures used to observe EIT. As mentioned in [11], common experiments involving EIT typically center around the storage medium. The two components of the experimental apparatus are shown in Figure 3.1. The workhorse of our experiment, as previously discussed, is a cell of gaseous ^{85}Rb atoms. A single distributed feedback laser of wavelength 780 nm drives the entire system through a network of wave plates and mirrors. However, the system we desire to study consists of two laser frequencies that must be both tuned near two-photon resonance and be mutually coherent. This is accomplished with the use of a Brimrose acousto-optic frequency shifter (AOFS), which is used to provide a blue and redshifted, pump and probe beam, respectively. The pump beam is vertically polarized before being routed to a non-polarizing beam splitter where it will align with the probe beam. Meanwhile, the probe beam passes through an Isomet acousto-optic modulator (AOM), which provides a scanning and intensity-control mechanism with the appropriate tuning of an AOM driver. The probe beam is horizontally polarized before aligned in a co-propagating manner with the pump beam. The non-polarizing beam splitter allows the two beams to remain cross-polarized as they transmit through the ^{85}Rb cell. Ample space is provided between the non-polarizing beam splitter and the cell for a removable beam expansion apparatus. A polarizing beam splitter filters the exiting, coupled beam, allowing the probe beam to be collected in the aperture of a photodiode detector and observed on a Tektronix Mixed Signal Oscilloscope.

To ensure the two laser frequencies are each on single photon resonance, 5% of the beam is picked off and routed to the saturated absorption spectroscopy (SAS) experiment. The SAS apparatus involves two weak, forward-propagating probe beams, and one strong, reverse-propagating pump beam. The two probe beams are aligned parallel to each other and transit through a ^{85}Rb cell before being measured with a photodiode detector. The pump beam, which is propagating in the reverse direction of the probe beams, is aligned such that it overlaps with one of the probe beams.

3.1 Techniques and Procedures

Various techniques and procedures were used throughout the evolution of this thesis to confirm or deny the presence of EIT, among other expected results. The following subsections highlight the most relevant and useful techniques for error avoidance.

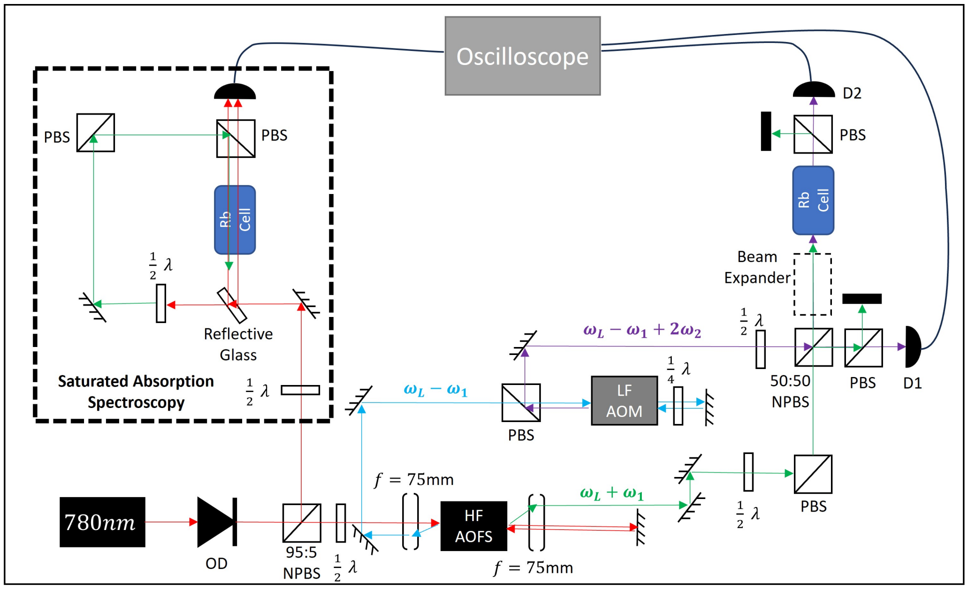

Figure 3.1. Table-top optical schematic for SAS and EIT.

3.1.1 Saturated Absorption Spectroscopy

The objective of SAS is to lock a laser onto the frequency of a particular hyperfine atomic transition. We are interested in the $5^2S_{1/2}\ F = 2 \longrightarrow 5^2P_{3/2}\ F' = 3$, where the prime signifies an excited state transition, which can be visualized in Figure 3.2. When the laser is tuned to resonance, the atoms absorb the energy and transmittance drops resulting in absorption dips as the laser is scanned across the resonance frequency. However, atoms at room temperature are traveling at many different velocities and thus experience a Doppler-broadening effect. To reveal the hyperfine structure, a strong counter-propagating pump beam is configured to spatially overlap with a probe beam. In such a configuration, the atom *sees* two lasers fields with opposite Doppler-shift and hence the two fields are not in-resonance at the same time. However, for atoms in the zero-velocity group, the Doppler shift is small, and the atom *sees* two laser fields that are both on resonance. The pump field excites the atoms, which then cannot absorb light from the pump. This results in an enhancement of the transition (i.e., transmission peaks). Since this effect only occurs for atoms with small Doppler-shift, it is a convenient way to determine the natural frequency of a transition (i.e., without Doppler-broadening) and to confirm the laser is operating in the appropriate linewidth where EIT may be found. Section 4.1 applies this in a lab environment and provides data in Figures 4.1 and 4.2.

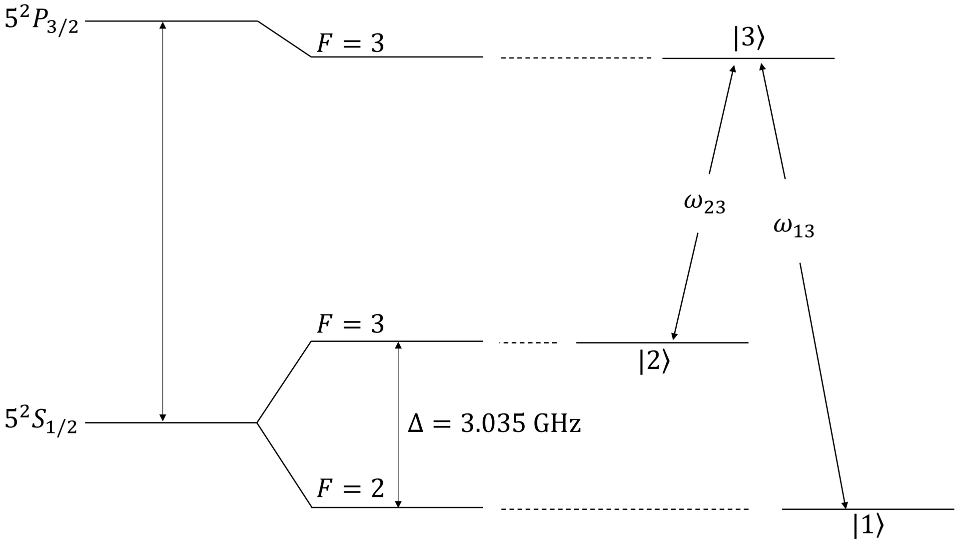

Figure 3.2. Beat frequency relationship of the hyperfine structure ground states, $|1\rangle$ and $|2\rangle$. Adapted from [13]

3.1.2 Acusto-Optic Frequency Shifter and Modulator

There are multiple methods to ensure that the beat frequency (e.g., the difference in the two laser frequencies) is close to or on two-photon resonance. In our apparatus, we chose to implement a double-pass technique through the Brimrose AOFS, which provides the desired beat frequency. Another common technique is to implement an Electro-Optic Modulator as discussed in [18].

In the AOFS scheme, the incident optical beam passes through the internal quartz crystal of the AOFS. The optical beam's first-order diffraction is shifted in frequency by the RF controlled acoustic carrier frequency. If the acoustic carrier is incident on the optical beam in the propagation direction of the beam, the first order diffraction is blueshifted. Conversely if it is in the opposite direction, the first order diffraction is redshifted. This mechanism enables us to achieve our desired beat frequency between the blue and redshifted beams, or pump and probe beams, respectively. The probe beam is routed through an additional low-frequency AOM because we need to scan across the resonant frequency without altering the pump beam. Again, we orient the probe beam in a double-pass configuration because the incident angle depends on the radio frequency driving the AOM; but the double-pass configuration removes this dependence, allowing us to scan the probe frequency without changing either the pump frequency or the alignment of the pump and probe on top of each other. We establish our desired acoustic carrier frequency in the following manner:

$$\Delta = (\omega_L + \omega_{HF}) - (\omega_L - \omega_{HF} + 2\omega_{LF}), \tag{3.1}$$

$$\Delta = 2(\omega_{HF} - \omega_{LF}), \tag{3.2}$$

$$\omega_{HF} = \frac{\Delta}{2} + \omega_{LF}, \tag{3.3}$$

where Δ has been implicitly measured and documented in [13], ω_{LF} is the center frequency of the Isomet AOM given in the product data sheet, and ω_{HF} is the acoustic carrier frequency required for the Brimrose AOFS. The specifications for the Isomet AOM (model number 1205-1118) indicates that the preferred driving frequency is 80 MHz and so we scan around this value. The resulting value for the driving freqency of the AOFS is 1597.866 MHz.

3.1.3 Modulation Generation

An Arbitrary Waveform Generator (AWG) is used to produce a Gaussian pulse with a slowly varying envelope and a Gaussian pulse with amplitude modulation. The Agilent Intuilink Waveform Editor program allows the user to create an arbitrary waveform to upload on an Agilent/Keysight 33220A AWG. The MATLAB script provided in Appendix A.4 is used to generate our Gaussian pulses and allows us to manipulate the pulse characteristics as needed. This proved to be a very simple and reliable method to shape the probe beam amplitude.

3.1.4 Determining Time Delay

The goal of this thesis is to predict and observe effects caused by propagation of a modulated pulse signal through an EIT medium. To do so, it makes sense to compare the output pulse, measured after the storage medium, to the input pulse, measured before the storage medium.

In our experimental scheme, we use two photodiode detectors. One detector (labeled D1 in Figure 3.1), is positioned to capture the input pulse from the combined signal exiting the 50:50 non-polarizing beam splitter just before the beam expansion device. The output pulse is captured by detector two (denoted by D2 in Figure 3.1) positioned on the far side of the storage medium. The oscilloscope is triggered by the output of the AWG such that the two signals are recorded simultaneously. Since the pulse incident on D1 has not gone through the cell, it will not be delayed. But the pulse incident on D2 may have suffered a delay due to the light slowing effect we are looking for.

The oscilloscope exports the signals in a comma-separated value format, which is analyzed with the MATLAB script detailed in Appendix A.1. Initially, the noisy signals are filtered with the wavelet denoising procedure outlined in Appendix A.2. A goodness-of-fit test applies the best fitting method to the recorded data. This process allows us to better synthesize the data; however, we acknowledge that the procedure of signal processing may inherently add factors of error and is considered when interpreting the results.

Lastly, we approach the time delay calculations by considering the cross-correlation of the input and output signals. After computing the cross-correlation, the maximum of the correlation function indicates the moment in time where the two signals are most closely aligned, i.e., the temporal distance one signal is delayed with respect to the other:

$$\tau_{\text{delay}} = \mathbf{argmax}\Big((f * g)(t)\Big), t \in \mathbb{R}. \tag{3.4}$$

3.2 Difficulties and Resource Shortfalls

The majority of difficulties experienced throughout this process generally pertain to the sensitive nature of beam alignment. In particular, the laser produces a 1-mm diameter beam, which is manipulated in size and position depending on the requirement of the optics. Specifically, to optimize the the efficiency of the Brimrose AOFS, the light needs to be focused onto the 0.076 mm active area of the modulator. To accomplish this, we positioned two large spheres on either side of the AOFS to focus the laser and simultaneously collimate the shifted beams.

The internal crystal of the AOFS induces additional unwanted effects. The incident optical beam can be reflected or refracted from either side of the crystal in such a way as to overlap with the first-order diffraction. In order to minimize the reflection or refraction and maximize the intensity of the first-order diffraction, we pulsed the AOFS radio frequency while tuning the x-y-z axes of the modulator during the set up phase. This approach allowed us to distinguish the desired beam from the unwanted beam.

An alternative approach that was considered includes the use of two Brimrose AOFS devices driven in tandem to produce the two desired frequencies from a single laser. However, due to time and existential logistical constraints (including the likely need to phase lock the two different RF sources), this schematic was not pursued further. While this approach does have the drawback of requiring more physical space, it has the advantage of less reflection and refraction interference.

THIS PAGE INTENTIONALLY LEFT BLANK

CHAPTER 4:
Data Collection and Analysis

Data collection was performed across multiple days. During each iteration of collection, operational procedures were standardized to minimize as much deviation in component performance as possible. However, we note that existential uncertainty exists, albeit relatively small, among collection efficiency of the detectors and stability of the laser source to frequency drift.

4.1 Absorption Spectroscopy

These data were collected while using the SAS component of the experimental apparatus detailed in Figure 3.1 and described in the surrounding text. The purpose of these data are to identify the absorption spectrum of ^{85}Rb and tune the pump beam to the appropriate transition frequency. Since our cell is not isotopically pure, we expect to see four D-Line transitions comprised of both the 85 and 87 isotopes. Our findings are presented in Figure 4.1.

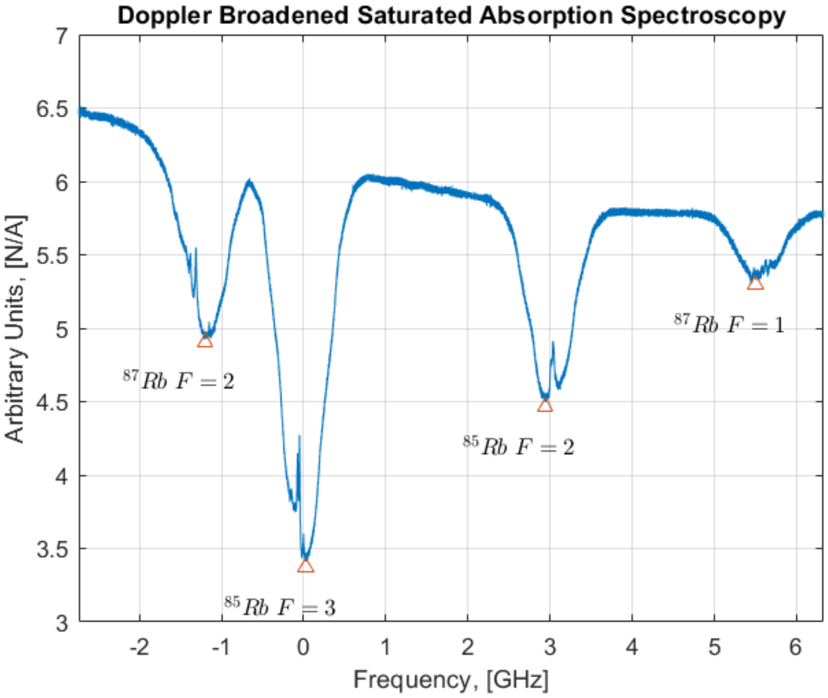

Figure 4.1. Laser transmission vs frequency. Frequency is centered on the $F = 3$ fine level. Scanning reveals all four sets of D2 lines. The absorption spectrum is Doppler-broadened because the storage medium consists of atoms traveling with a Boltzmann distribution of velocities.

Our scan reveals the fine structure of the rubidium cell; however, the Doppler-broadening effect conceals the hyperfine structure, which is more important to this study. As addressed in Section 3.1, a counter-propagating beam is introduced to produce a Doppler-free hyperfine resolution of the rubidium energy structure in Figure 4.2.

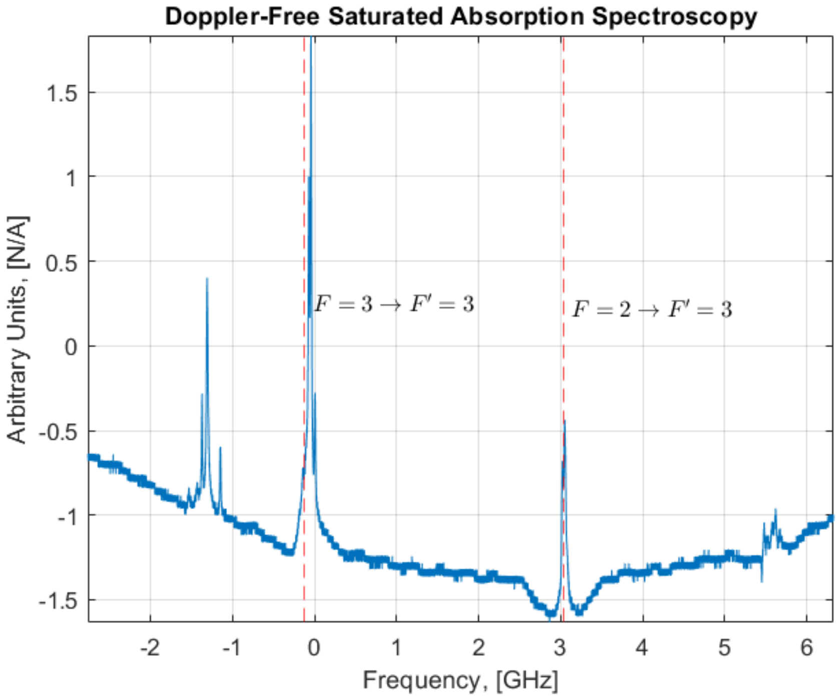

Figure 4.2. Laser transmission measured in arbitrary units vs frequency. Frequency is centered on the $F = 3$ fine level. A counter-propagating beam is used to reveal the hyperfine energy structure in this Doppler-free absorption spectrum.

More closely, Figure 4.3 reveals the hyperfine transitions of $F = 3 \longrightarrow F'$ for reference. We isolate the $F' = 3$ energy level for reasons previously discussed in Chapter 2. Likewise, we identify a similar transition for $F = 2 \longrightarrow F' = 3$, although not depicted.

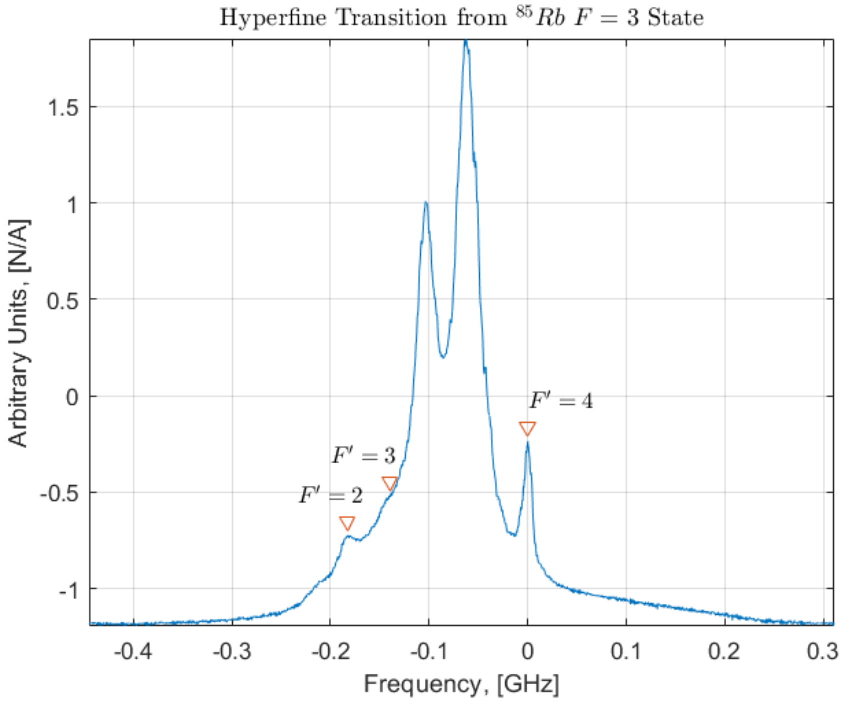

Figure 4.3. Laser transmission measured in arbitrary units vs frequency specifically scanning over the $F = 3 \rightarrow F'$ energy transitions. Unlabeled peaks indicate crossover resonances where the laser frequency is halfway between two different hyperfine transitions. Their details are unrelated to the topic of this thesis; however, [24] provides more information for the curious reader.

The laser frequency is controlled by a voltage ramp. By measuring the spectrum as a function of the voltage ramp, we can determine the appropriate voltage that corresponds to the resonance frequency. The pump beam will then drive the $|2\rangle \rightarrow |3\rangle$ transition, modifying the absorptive properties of the ^{85}Rb particles.

4.2 EIT Response

Now that the pump beam has been tuned to the appropriate transition, we divert our attention to the probe beam. The ISOMET AOM allows us to independently scan a small frequency range including the expected resonance frequency of the $|1\rangle \rightarrow |3\rangle$ transition. A second voltage ramp drives the AOM to scan 16.0 ± 0.1 MHz around a center frequency of 80 MHz. Equation (2.48a) tells us that as the detuning approaches zero, $\delta_1 \rightarrow 0$, the absorption of the probe beam also approaches zero, i.e., we expect to observe a spike in transmission when the pump beam is present. Our results are depicted by the trace in Figure 4.4.

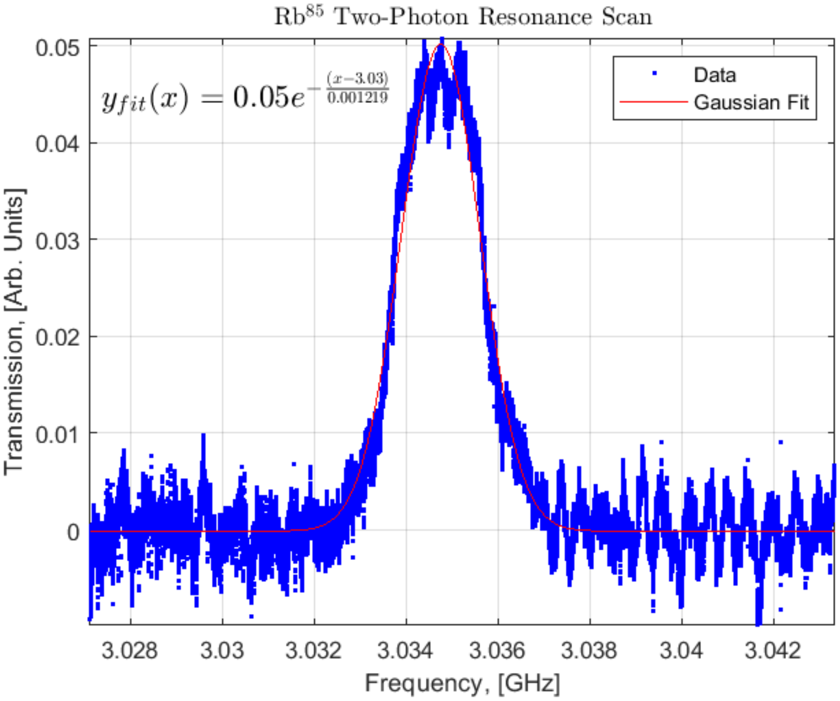

Figure 4.4. Laser transmission measured in arbitrary units vs frequency. The x-axis is centered on the expected beat frequency, 3.035 GHz, of the two ground-state transitions. On resonance, we expect an increase in transmission because the pump beam is optically modifying the absorptive properties of the Rubidium atom through the EIT effect, allowing the probe beam to propagate through the storage medium with increased transmission for a range of frequencies as observed here. The linewidth of this feature is measured to be 2.3 ± 0.1 MHz.

We know EIT to be a sub-natural linewidth phenomenon, whereas the natural full width at half maximum linewidth of ^{85}Rb is 6 MHz [13], [17]. The linewidth of our transmission peak is measured to be 2.3 ± 0.1 MHz, supporting the conclusion that the feature is indeed caused by the EIT effect. Additionally, the size of our transparency window is defined by the linewidth, in turn, constraining the bandwidth of any probe signals to be stored in the medium.

4.3 Controlled Time Delay in EIT

By measuring the response of the probe beam in the EIT condition as a function of the control volatge, we are able to precisely tune the probe beam in much the same manner as the tuning of the pump beam described in the previous section. Equation (2.51) indicates that the group velocity of a probe beam is controllable while transiting an EIT medium on two-photon resonance. We expect the control factor to behave like (2.52). To measure the slow light phenomenon, we seek to capture time delay data from the probe beam using (3.4). The signal is recorded at two instances in time, before the storage medium and after the storage medium. Their information is cross-correlated and a time delay is generated across a range of pump beam intensities.

Prior to observing time delays in the transmitted pulse, it is imperative we understand the effect our Isomet AOM will have on the probe beam. To achieve the response we desire, we need to operate the AOM in a linear region when a control voltage is applied to the probe beam intensity. Thus, we recorded the probe intensity as a function of the intensity control voltage and chose a region between the two dashed lines as being linear with the largest response in Figure 4.5.

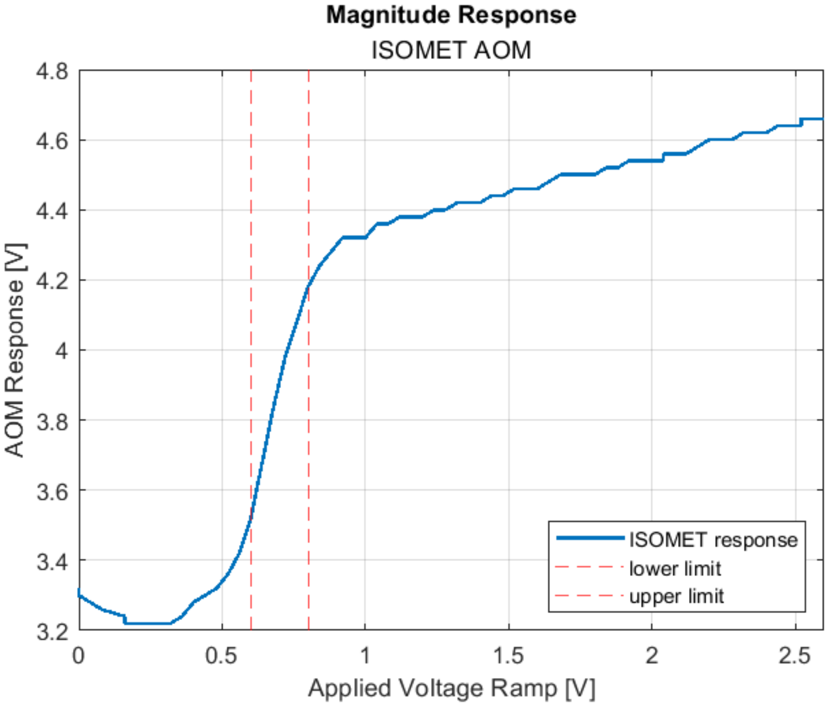

Figure 4.5. The magnitude response of the ISOMET AOM is recorded as a function of the applied voltage.

We begin with a simple continuous sinusoidal modulation scheme shown in Figure 4.6a and apply it to the probe beam. In Figure 4.7a, we note that the majority of the modulation energy is present at frequencies less than 2 kHz and much less than the EIT transparency window. To verify the light-slowing effect exists in our current experimental set up, we attempt to re-create the results published by M. Kash et al. [25]. Figure 4.8 demonstrates four cases in which a delay is observed while comparing the input to the output signal, supporting the existence of controllable light-slowing. We repeat this process and report a decaying exponential trend across many trials in Figure 4.9a, which aligns with Kash et al. However, we note that our results are an order of magnitude less. This is likely a result of a thinner EIT linewidth achieved by Kash et al., leading to more pronounced delays. We construct the remaining modulation schemes and determine their power spectral densities in Figure 4.6 and 4.7. Repeating the same process, we make note of the results.

Our time delay results for all modulation schemes are recorded in Figure 4.9. In agreement with our theoretical predictions, we observe exponentially decaying time delay in all of the applied modulation schemes except the square pulse. In fact, to achieve the EIT delays we are after, a slowly varying envelope with power spectral densities tightly coupled to the lower frequency range is ideal. The sharp transitions of a square pulse distribute the signal energy over a large bandwidth, likely exceeding the bounds of the EIT transparency window, as seen in Figure 4.7b and leading to negligible time delay. As for the other three cases, the data appear to be in fairly good agreement with (2.52) from Chapter 2. While the data provide promising results and are supported by similar work [25], there are a few values that appear to differ by a sizable margin. To confirm a dependence on the pump strength, we discuss future outlook in Chapter 5.

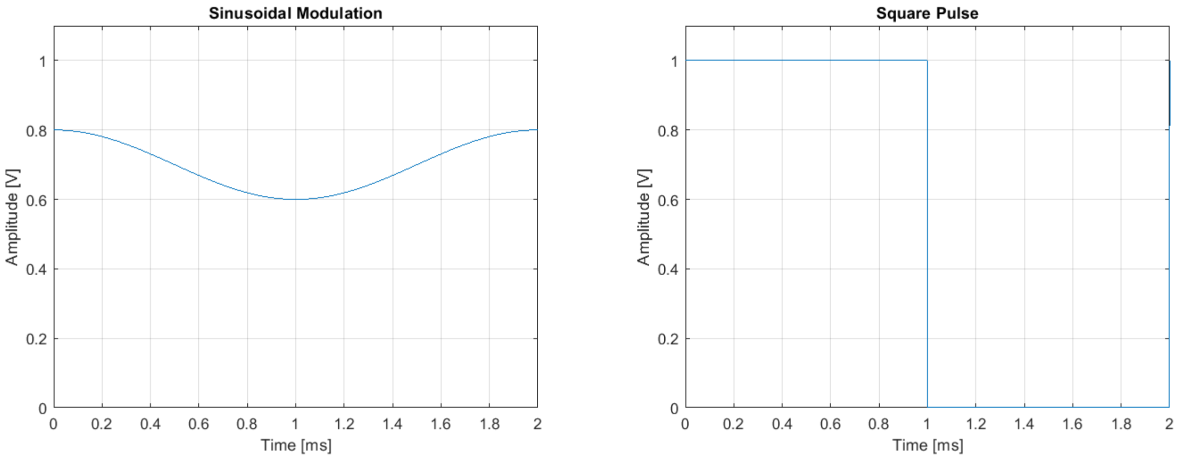

(a) 500 Hz Sinusoid (b) 500 Hz Square Pulse

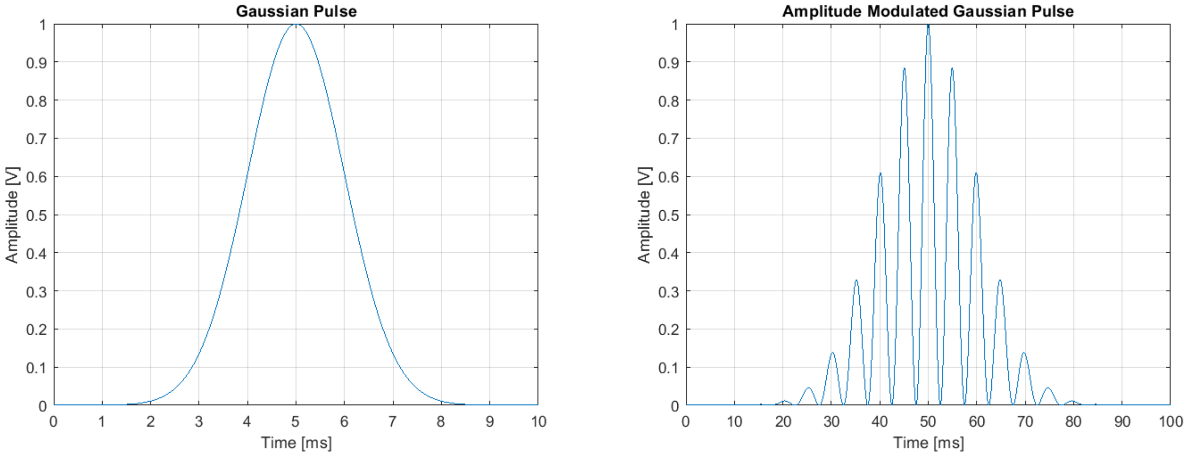

(c) 100 Hz Gaussian Pulse (d) 10 Hz Gaussian Pulse with Amplitude Modulation

Figure 4.6. Modulation schemes applied to the probe beam.

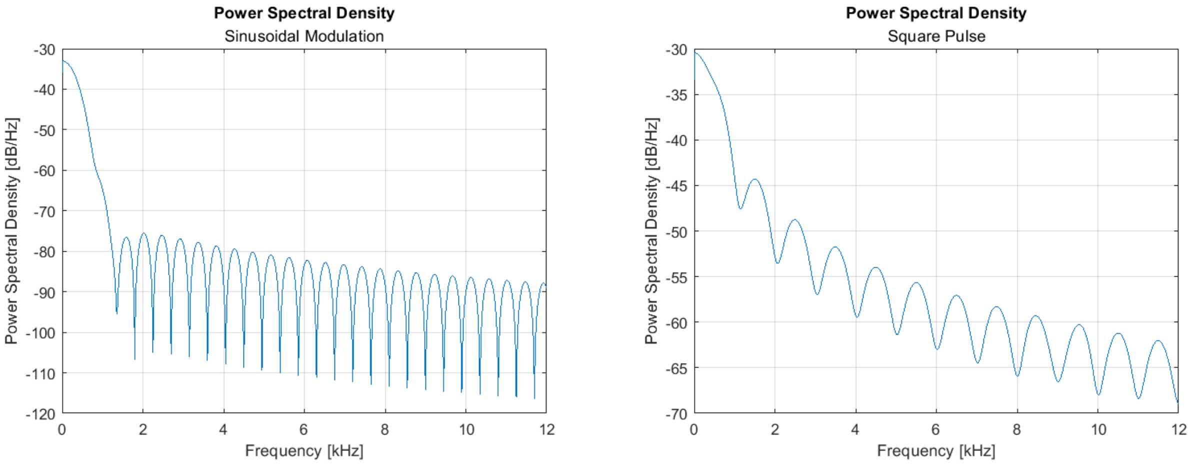

(a) 500 Hz Sinusoid

(b) 500 Hz Square Wave

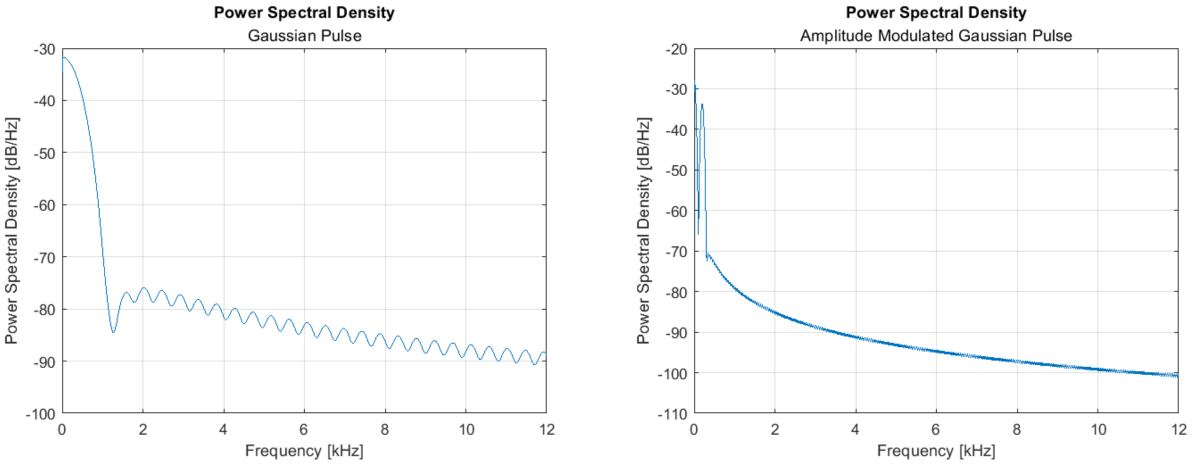

(c) 100 Hz Gaussian Pulse

(d) 10 Hz Gaussian Pulse with Amplitude Modulation

Figure 4.7. Power spectral densities of the applied modulation schemes.

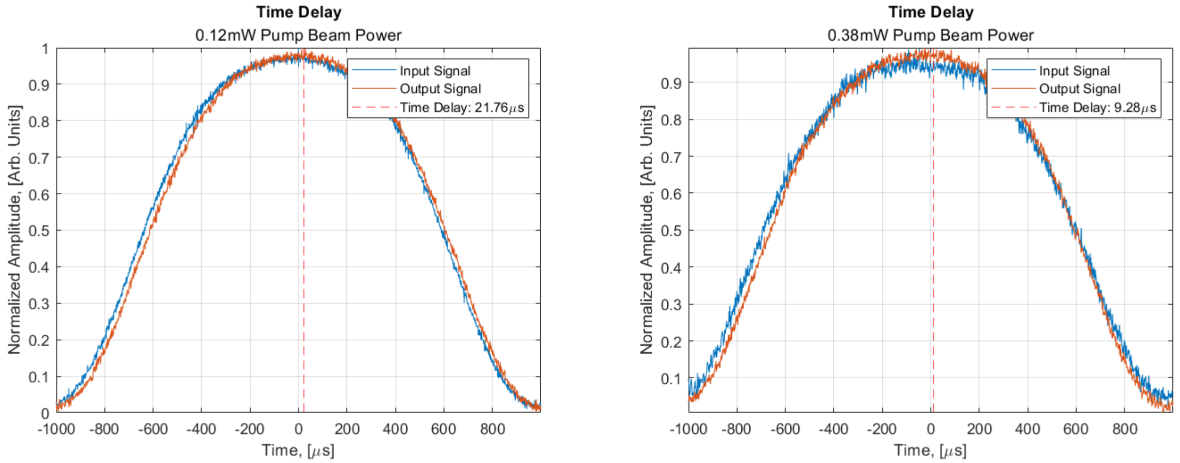

(a) Time Delay with 0.12 mW Pump Beam Power (b) Time Delay with 0.38 mW Pump Beam Power

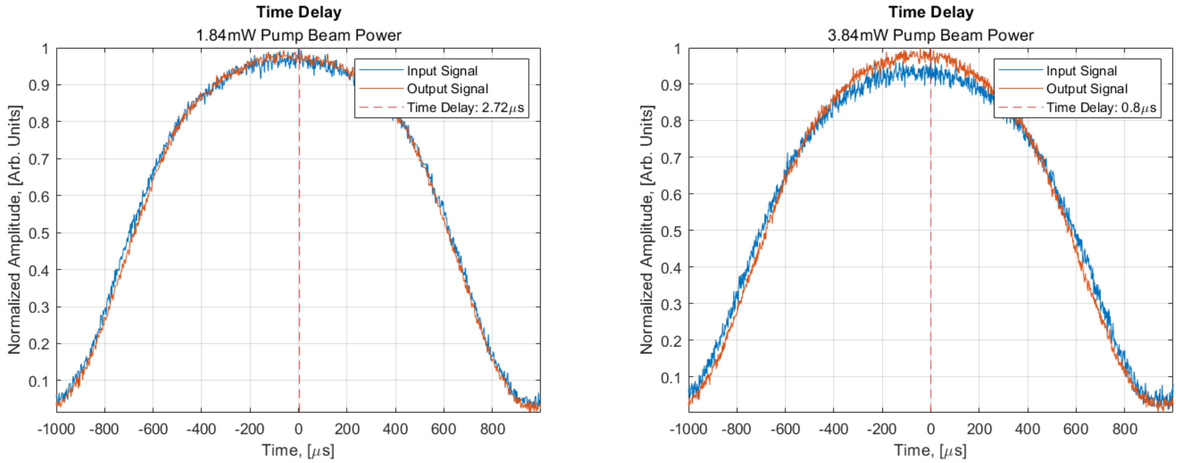

(c) Time Delay with 1.84 mW Pump Beam Power (d) Time Delay with 3.84 mW Pump Beam Power

Figure 4.8. Time delayed sinusoidal modulation comparing the input signal to the output signal.

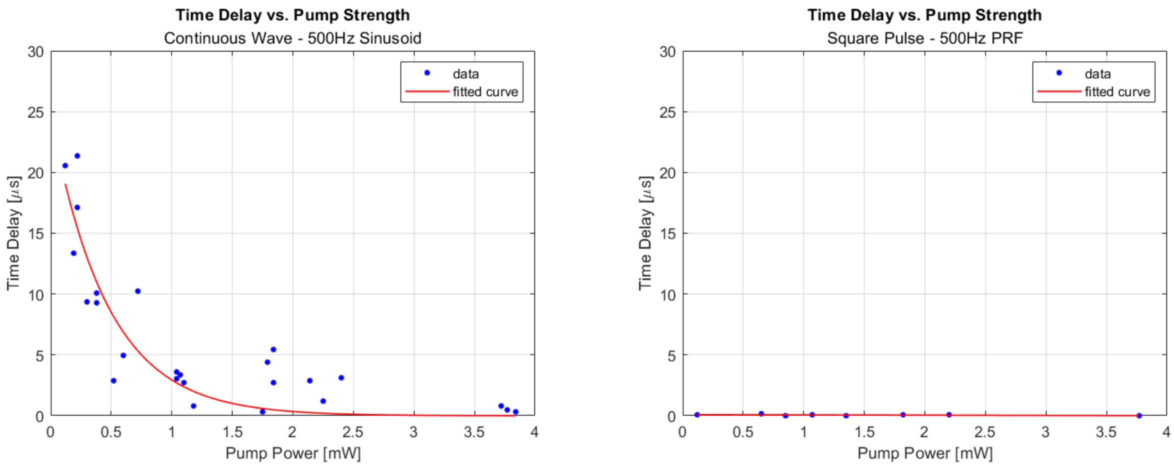

(a) 500 Hz Sinusoid (b) 500 Hz Square Wave

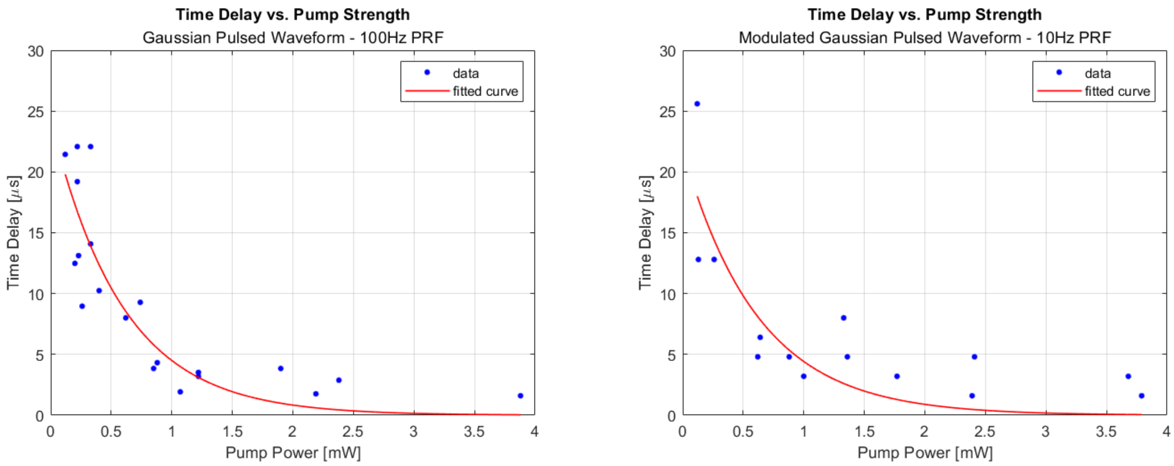

(c) 100 Hz Gaussian Pulse (d) 10 Hz Gaussian Pulse with Amplitude Modulation

Figure 4.9. Time delay as a function of pump strength.

CHAPTER 5:
Conclusions

Although the advent of the field of quantum mechanics dates back to the early 1900s, we continue to find new applications that carry the promise of revolutionizing existing technologies. With increased investments, the field has rapidly progressed to the point where quantum devices have emerged and are becoming commercialized. Early prototypes of quantum sensors and quantum communication systems are being fielded, and even rudimentary quantum computers are beginning to make an appearance on the market. Needless to say, further research and development are needed to fully exploit the promise of quantum technologies.

The goal of this thesis is to lay the foundation for continued research at Naval Postgraduate School (NPS) to explore the efficacy of EIT-based optical memory. In doing so, we accomplished three main achievements: the successful establishment of a working EIT apparatus, the development of the means to manipulate and transmit a signal beam, and the construction of a framework for continued success in realization of quantum memory.

The experimental apparatus has been shown to clearly produce an EIT response with the instruments provided; however, it is not optimal. Further work can be done to amplify the probe signal by considering alternative beam alignment methods. Initial difficulty was experienced while attempting to combine the probe and pump signal into a single-mode, polarization-maintaining fiber optic cable. While combining the two beams into the fiber has the advantage that the two beams emerge automatically mode-matched, polarization mixing in the fiber caused bleed-through of the pump into the probe detection channel, corrupting the output signal. As a rudimentary solution, we chose to move forward with polarized beam-splitting cubes, which enhanced the experiment for two reasons: first, we were able to achieve nearly perfect cross-polarization and second, we avoided the losses in beam power associated with coupling losses into the fiber. The trade-off, however, was beam alignment through the storage medium. A precisely aligned co-propagating beam will amplify the two-photon EIT response and decrease its linewidth. Slowed group velocity is inversely proportional to linewidth, therefore resulting in increased (and hence more easily detectable) delays. Achieving delays on the order of milliseconds should be possible if the linewidth can be reduced by a few orders of magnitude. Furthermore, manipulating environmental factors such as applied heat sources may also lead to greater delays and is worth considering. Increasing the temperature of the storage medium will proportionally increase atomic density and by extension promote a greater chance of particle interaction with the laser beam. But care should be taken as the heating elements will produce a magnetic field that can interfere with the response.

In this thesis, four modulation schemes were applied in sequential order to assess the impact of the EIT medium on the response of the probe beam. While our initial results are promising, continued data collection is recommended to achieve a statistically large enough sample size for verification. Moreover, the system is capable of transmitting data that provide significant opportunity to study the process of signal recovery and possible error correction methodologies. This will be increasingly important as the apparatus develops to a state in which the probe signal is successfully stored inside the EIT medium.

Lastly, this work has laid the foundation for continued cooperation on quantum technologies between the Departments of Electrical Engineering and Physics at NPS. Engineers have historically approached complex problems pragmatically; however, the idiosyncratic characteristics of quantum phenomena require deeper investigations that the domain of physicists are capable of providing. Together, significant progress can be made toward advancing the state of quantum technologies.

APPENDIX A:

A.1 Modulated EIT

```
%% Modulated EIT
% This function processes the input and output probe signal to
   determine a time delay based on its cross correlation.

function [Tdelay,D] = ModulatedEIT(Data,Ts)
% Values to map Input/Output to
a = 1;
b = 0;
i = 1:16;

% Raw Data
Time = Data(:,1);
input = ( Data(:,2) );
output = ( Data(:,7) );
modulation = Data(:,4) ;

% processed input signal (denoized)
proc_input = Preprocess( input, i );

% processed output signal (denoized)
proc_output = Preprocess( output, i );

% amplitude modulation driving the AOM
proc_modulation = Preprocess( modulation, i );

% Rescale Input
m = (b - a) / (min(proc_input) - max(proc_input));
n_proc_input = m*(proc_input)-m*min(proc_input) + b;

% Rescale Output
```

```
m = (b - a) / (min(proc_output) - max(proc_output));
n_proc_output = m*(proc_output)-m*min(proc_output);

% find max peak
ii = find( n_proc_input == max(n_proc_input) );
%[pks,locs] = findpeaks(n_proc_input);%,"MinPeakProminence",0.65)
   ;
%ii = find( pks == max(pks));

% center the input pulse
Tdur = 1/500; % pulse duration
newTime = -Tdur/2:Ts:Tdur/2-Ts;
L = length(newTime);

if ii-L/2 > 0 && ii+L/2-1 < length(Time)
    b = ii-L/2;
    e = ii+L/2-1;
elseif ii-L/2 > 0 && ii+L/2-1 > length(Time)
    b = ii-3*L/2;
    e = ii-L/2-1;
else
    b = ii+L/2;
    e = ii+3*L/2-1;
end

% cross correlation (b:e)
[Rx lag] = xcorr(n_proc_input,n_proc_output);

% Plot Figures
figure()
plot(newTime,proc_output(b:e)); grid on, hold on
plot(newTime,proc_input(b:e))
hold off
axis("tight")
title('No Scaling - Processed Signals')
legend("Output","Input")
```

```
figure()
plot(newTime,n_proc_output(b:e)); grid on, hold on
plot(newTime,n_proc_input(b:e))
hold off
axis("tight")
title('Normalized - Processed Signals')
legend("Output","Input")

% Compute Time Delay
[xa,ya,D] = alignsignals(n_proc_input(b:e),n_proc_output(b:e),"
   Method","xcorr");
Tdelay = D*Ts;

end
```

A.2 Signal Processing

```
%% Signal Processing
% This function runs the input through various signal estimation
   schemes and uses a chi-square test to determine which
   estimation method produces the best result.

function y = Preprocess(x,opts)

% Descriptive Statistics
count = length(x);
meanI = mean(x);
stdvI = std(x);
CV = chi2inv(0.95,count-1);

L = length(opts);
hold = [zeros(count,L)];
for inc = 1:L
    switch opts(inc)
        case 1
```

```
%fprintf('We are denoising the signal with case %.0f.\n\n
   ',opts(inc))
hold(:,1) = wdenoise(x, 4,
   UU
   ...
'Wavelet', 'db3', ...
'DenoisingMethod', 'Bayes', ...
'ThresholdRule', 'Median', ...
'NoiseEstimate', 'LevelIndependent');

case 2
%fprintf('We are denoising the signal with case %.0f.\n\n
   ',opts(inc))
hold(:,2) = wdenoise(x, 6, ...
'Wavelet', 'db3', ...
'DenoisingMethod', 'Bayes', ...
'ThresholdRule', 'Median', ...
'NoiseEstimate', 'LevelIndependent');

case 3
%fprintf('We are denoising the signal with case %.0f.\n\n
   ',opts(inc))
hold(:,3) = wdenoise(x, 10, ...
'Wavelet', 'db3', ...
'DenoisingMethod', 'Bayes', ...
'ThresholdRule', 'Median', ...
'NoiseEstimate', 'LevelIndependent');

case 4
%fprintf('We are denoising the signal with case %.0f.\n\n
   ',opts(inc))
hold(:,4) = wdenoise(x, 4, ...
'Wavelet', 'db6', ...
'DenoisingMethod', 'Bayes', ...
'ThresholdRule', 'Median', ...
'NoiseEstimate', 'LevelIndependent');
```

```
case 5
%fprintf('We are denoising the signal with case %.0f.\n\n
   ',opts(inc))
hold(:,5) = wdenoise(x, 6, ...
'Wavelet', 'db6', ...
'DenoisingMethod', 'Bayes', ...
'ThresholdRule', 'Median', ...
'NoiseEstimate', 'LevelIndependent');

case 6
%fprintf('We are denoising the signal with case %.0f.\n\n
   ',opts(inc))
hold(:,6) = wdenoise(x, 10, ...
'Wavelet', 'db6', ...
'DenoisingMethod', 'Bayes', ...
'ThresholdRule', 'Median', ...
'NoiseEstimate', 'LevelIndependent');

case 7
%fprintf('We are denoising the signal with case %.0f.\n\n
   ',opts(inc))
hold(:,7) = wdenoise(x, 4, ...
'Wavelet', 'db12', ...
'DenoisingMethod', 'Bayes', ...
'ThresholdRule', 'Median', ...
'NoiseEstimate', 'LevelIndependent');

case 8
%fprintf('We are denoising the signal with case %.0f.\n\n
   ',opts(inc))
hold(:,8) = wdenoise(x, 6, ...
'Wavelet', 'db12', ...
'DenoisingMethod', 'Bayes', ...
'ThresholdRule', 'Median', ...
'NoiseEstimate', 'LevelIndependent');
```

```
case 9
%fprintf('We are denoising the signal with case %.0f.\n\n
   ',opts(inc))
hold(:,9) = wdenoise(x, 10, ...
'Wavelet', 'db12', ...
'DenoisingMethod', 'Bayes', ...
'ThresholdRule', 'Median', ...
'NoiseEstimate', 'LevelIndependent');

case 10
%fprintf('We are denoising the signal with case %.0f.\n\n
   ',opts(inc))
hold(:,10) = wdenoise(x, 4, ...
'Wavelet', 'sym4', ...
'DenoisingMethod', 'Bayes', ...
'ThresholdRule', 'Median', ...
'NoiseEstimate', 'LevelIndependent');

case 11
%fprintf('We are denoising the signal with case %.0f.\n\n
   ',opts(inc))
hold(:,11) = wdenoise(x, 6, ...
'Wavelet', 'sym4', ...
'DenoisingMethod', 'Bayes', ...
'ThresholdRule', 'Median', ...
'NoiseEstimate', 'LevelIndependent');

case 12
%fprintf('We are denoising the signal with case %.0f.\n\n
   ',opts(inc))
hold(:,12) = wdenoise(x, 10, ...
'Wavelet', 'sym4', ...
'DenoisingMethod', 'Bayes', ...
'ThresholdRule', 'Median', ...
'NoiseEstimate', 'LevelIndependent');
```

```
    case 13
    %fprintf('We are denoising the signal with case %.0f.\n\n
       ',opts(inc))
    hold(:,13) = wdenoise(x, 4, ...
        NoiseEstimate="LevelDependent");

    case 14
    %fprintf('We are denoising the signal with case %.0f.\n\n
       ',opts(inc))
    hold(:,14) = wdenoise(x, 6, ...
        NoiseEstimate="LevelDependent");

    case 15
    %fprintf('We are denoising the signal with case %.0f.\n\n
       ',opts(inc))
    hold(:,15) = wdenoise(x, 10, ...
        NoiseEstimate="LevelDependent");

    case 16
    %fprintf('We are denoising the signal with case %.0f.\n\n
       ',opts(inc))
    hold(:,16) = wdenoise(x);

end

% Does the Mean of the processed signal fall within 95% CI?
SEM = std(x)/sqrt(length(x));                % Standard Error
ts = tinv([0.025  0.975],length(x)-1);       % T-Score
CI = mean(x) + ts*SEM;                       % Confidence
   Intervals
meanY = mean(hold(:,inc));
% fprintf('The CI for case %.0f is between %.6f - %.6f.\n\n',
   opts(inc),CI)
% fprintf('The mean of the processed signal is: %.6f.\n\n',
   meanY)
```

```
    % goodness of fit
    chi1(inc) = sum((x-hold(:,inc)).^2./hold(:,inc));
    % fprintf('The critical value of the chi square test is: %.4f
       .\n\n',CV)
    % fprintf('The chi square score is: %.4f.\n\n',chi1(inc))

end
this = find(chi1 == min(chi1),1,"first");
fprintf('Case %.0f produced the estimated signal with the best
   fit.\n\n', this)
y = hold(:,this);

end
```

A.3 Line Width

```
%% LineWidth
% This function synthesizes data collected from scanning across a
    frequency range and plots the response as a function of
   frequency to determine the EIT response.

function [LW] = LineWidth(Data,fmin,fmax)

% Data Parameters
ramp = Data(:,4);
low = find(ramp == min(ramp),1,'first');
hi = find(ramp == max(ramp),1,'last');
Time = Data(low:hi,1);
n = 0:1:length(Time)-1;
m = (fmax-fmin)/length(Time);
f = fmin + m*n;

% Denoise the signals
ramp = Preprocess( ramp(low:hi), 2);
Ref = Preprocess( Data(low:hi,7),2 );
```

```
EIT = Preprocess( Data(low:hi,2),2 );

% Remove bias
inc1 = 0.35*length(n);
inc2 = 0.7*length(n);
p1 = polyfit(f(1:inc1),EIT(1:inc1),1);
y1 = polyval(p1,f(1:inc2));
p2 = polyfit(f(inc2:end),EIT(inc2:end),1);
y2 = polyval(p2,f(inc2:end));
yy = [y1 y2];
y = EIT - yy.';


if mean(Ref) > mean(y)
    y = (y./Ref).';
else
    y = (Ref./y).';
end

% Determine FWHP
FWHP = (max(y)-y(1))/2+y(1);
ind = find(y >= FWHP);

% Compute Linewidth
LW = f(ind(end)) - f(ind(1));

% Apply a 1-term Gaussian Fit
gaussEqn = 'a*exp(-((x-b)/c)^2)+d';
startPoints = [0.9 3.035 1e-3 0.88]; % [ a b c d ]
excludedPoints = [];

f1 = fit(f'/1e9, y', gaussEqn,'Start', startPoints, 'Exclude',
   excludedPoints);

formatspec1 = '%.2f';
formatspec2 = '%.6f';
```

```
geqn = ['$y_{fit}(x)=', num2str(f1.a,formatspec1),'e^{-\frac{(x-'
   , num2str(f1.b,formatspec1),')}{', ...
    num2str(f1.c,formatspec2),'}}$'];

% Plot figure
figure()
plot(f1,f/1e9,y); hold on; grid on;
text(f(1000)/1e9,0.045,geqn,"Interpreter","latex","FontSize",14)
hold off

axis("tight")
title('Rb$^{85}$ Two-Photon Resonance Scan',"Interpreter","latex
   ")
xlabel('Frequency, [GHz]')
ylabel('Transmission, [Arb. Units]')
legend('Data','Gaussian Fit')

end
```

A.4 Modulation Scheme Generator

```
%% Sinusoid and Square Waveform Generator
% MATLAB m-file for generating a Sinusoid and Square Wave Signal.
clc, clear, close all,
% Constants
N = 10000;                  % Number of Samples
PRF = 500;                  % Pulse Repetition Frequency [Hz]
t_min = 0;                  % Minimum time value
t_max = 5*1/PRF;              % Maximum time value

% Time vector
t = linspace(t_min, t_max, N);
dt = abs(t(2)-t(1));

% Frequency vector
fs = 1/dt;
```

```
df = 1/(dt*N);
NFFT = 10*N;
f = fs*(-NFFT/2:NFFT/2-1)/NFFT;

% Sinusoidal Wave Equation
cw_sig = 0.7+0.1*cos(2*pi*PRF*t);
% Square Wave Equation
sqp = 0.5*(1+square(2*pi*PRF*t));

% Fourier Transform
CW = 1/sqrt(NFFT/N)*fftshift(fft(cw_sig,NFFT))*dt;
SQP = 1/sqrt(NFFT/N)*fftshift(fft(sqp,NFFT))*dt;

% Energy Check
Ecw = sum(cw_sig.*conj(cw_sig) * dt)
ECW = sum(CW.*conj(CW) * df)

Esqp= sum(sqp.*conj(sqp) * dt)
ESQP= sum(SQP.*conj(SQP) * df)

% Power Spectral Density
[Pcw, f1] = pwelch(cw_sig,[],[],NFFT,fs,"onesided");
[Psqp, f2] = pwelch(sqp,[],[],NFFT,fs,"onesided");

%%%%%%% FIG PLOTTING %%%%%%%
%%%%%%% TIME DOMAIN  %%%%%%%
figure()
plot(t/1e-3, cw_sig); grid on;
xlabel('Time [ms]');
ylabel('Amplitude [V]');
xlim([0 2])
ylim([0 1.1])
title('Sinusoidal Modulation');

figure()
plot(t/1e-3, sqp); grid on;
```

```
xlabel('Time [ms]');
xlim([0 2])
ylim([0 1.1])
ylabel('Amplitude [V]');
title('Square Pulse');
%%%%%%%%%%%%%%%%%%%%%%%%%%%
%%%%%%% FREQ DOMAIN %%%%%%%
figure()
plot(f/1e3, abs(CW)); grid on;
xlabel('Frequency [kHz]');
ylabel('Magnitude');
xlim([-5 5]);
title('Frequency Response','Sinusoidal Modulation');

figure()
plot(f/1e3, abs(SQP)); grid on;
xlabel('Frequency [kHz]');
ylabel('Magnitude');
xlim([-20 20]);
title('Frequency Response','Square Pulse');
%%%%%%%%%%%%%%%%%%%%%%%%%%%
%%%%%%%%%%% PSD %%%%%%%%%%%
figure()
plot(f1/1e3,pow2db(1/sqrt(NFFT/N)*Pcw)); grid on;
title('Power Spectral Density','Sinusoidal Modulation');
xlabel('Frequency [kHz]')
ylabel('Power Spectral Density [dB/Hz]');
xlim([0 12]);

figure()
plot(f2/1e3,pow2db(Psqp)); grid on;
title('Power Spectral Density','Square Pulse');
xlabel('Frequency [kHz]')
ylabel('Power Spectral Density [dB/Hz]');
xlim([0 12])
%%%%%%%%%%%%%%%%%%%%%%%%%%%
```

```
%%%%%%%%%%%%%%%%%%%%%%%%%%%
%% Gaussian and Amplitude Modulated Gaussian Pulse Waveform Generator
% MATLAB m-file for generating a Gaussian pulse
clc, clear, close all,
% Constants
N = 65536;                   % Optimal Number of points for AWG 33220A
t_min = 0;                   % Minimum time value
t_max = 10e-3;              % Maximum time value

% Parameters
t0 = (t_min+t_max)/2;            % Center time of the pulse
sigma = 0.1*abs(t_max-t_min);    % Standard deviation (width) of the pulse
omega = 2*pi*1e3;                % Modulation frequency
a = 1/(2 * sigma^2);

% Time vector
t = linspace(t_min, t_max, N);
dt = abs(t(2)-t(1));

% Frequency vector
fs = 1/dt;
df = 1/(N*dt);
NFFT = 10*N;
f = fs*(-NFFT/2:NFFT/2-1)/NFFT;

% Gaussian pulse equation
gaussian_pulse = exp(-a*(t - t0).^2 ).';%sqrt(a/pi)*
mod_gaussian_pulse = cos(omega*t.').^2.* gaussian_pulse;

% Fourier Transform
GP = 1/sqrt(NFFT/N)*fftshift(fft(gaussian_pulse,NFFT))*dt;
MGP = 1/sqrt(NFFT/N)*fftshift(fft(mod_gaussian_pulse,NFFT))*dt;
```

```
% Energy Check
Egp = sum(gaussian_pulse.*conj(gaussian_pulse) * dt)
EGP = sum(GP.*conj(GP) * df)

Emgp= sum(mod_gaussian_pulse.*conj(mod_gaussian_pulse) * dt)
EMGP= sum(MGP.*conj(MGP) * df)

% Power Spectral Density
[Pgp, f1] = pwelch(gaussian_pulse,[],[],NFFT,fs,"onesided");
[Pmgp, f2] = pwelch(mod_gaussian_pulse,[],[],NFFT,fs,"onesided");

%%%%%%% FIG PLOTTING %%%%%%%
%%%%%%% TIME DOMAIN  %%%%%%%
figure()
plot(t/1e-3, gaussian_pulse); grid on;
xlabel('Time [ms]');
ylabel('Amplitude [V]');
title('Gaussian Pulse');

figure()
plot(t/1e-3, mod_gaussian_pulse); grid on;
xlabel('Time [ms]');
ylabel('Amplitude [V]');
title('Amplitude Modulated Gaussian Pulse');
%%%%%%%%%%%%%%%%%%%%%%%%%%%
%%%%%%% FREQ DOMAIN %%%%%%%
figure()
plot(f/1e3, abs(GP)); grid on;
xlabel('Frequency [kHz]');
ylabel('Magnitude');
xlim([-1 1]);
title('Frequency Response','Gaussian Pulse');

figure()
plot(f/1e3, abs(MGP)); grid on;
xlabel('Frequency [kHz]');
```

```
ylabel('Magnitude');
xlim([-3 3]);
title('Frequency Response','Amplitude Modulated Gaussian Pulse');
%%%%%%%%%%%%%%%%%%%%%%%%%%%
%%%%%%%%%%% PSD %%%%%%%%%%%
figure()
plot(f1/1e3,pow2db(Pgp)); grid on;
title('Power Spectral Density','Gaussian Pulse');
xlabel('Frequency [kHz]')
ylabel('Power Spectral Density [dB/Hz]');
xlim([0 12]);

figure()
plot(f2/1e3,pow2db(Pmgp)); grid on;
title('Power Spectral Density','Amplitude Modulated Gaussian
   Pulse');
xlabel('Frequency [kHz]')
ylabel('Power Spectral Density [dB/Hz]');
xlim([0 12])
%%%%%%%%%%%%%%%%%%%%%%%%%%%
%%%%%%%%%%%%%%%%%%%%%%%%%%%
% Save Gaussian pulse as a CSV file
dlmwrite('gaussian_pulse.csv', gaussian_pulse, 'delimiter', ',',
   'precision', '%.6f');
dlmwrite('mod_gaussian_pulse.csv', mod_gaussian_pulse, 'delimiter
   ', ',', 'precision', '%.6f');
```

THIS PAGE INTENTIONALLY LEFT BLANK

List of References

[1] M. Bogobowicz, S. Gao, M. Masiowski, N. Mohr, H. Soller, R. Zemmel, and M. Zesko. (2023). Quantum technology sees record investments, progress on talent gap. [Online]. Available: https://www.mckinsey.com/capabilities/mckinsey-digital/our-insights/quantum-technology-sees-record-investments-progress-on-talent-gap/

[2] Congressional Research Service. (2022, April). *Defense Primer: Quantum Technology*. [Online]. Available: https://crsreports.congress.gov/

[3] C. H. Bennett and G. Brassard, "Quantum cryptography: Public key distribution and coin tossing," in *Proceedings of IEEE International Conference on Computers, Systems, and Signal Processing*, India, 1984, p. 175.

[4] A. Nellis, "The quantum internet," https://news.uchicago.edu/explainer/quantum-internet-explained, December 2022, (Accessed on 08/10/2023).

[5] U.S. Department of Energy, "U.S. Department of Energy unveils blueprint for the quantum internet," https://www.energy.gov/articles/us-department-energy-unveils-blueprint-quantum-internet-launch-future-quantum-internet, July 2020, (Accessed on 08/10/2023).

[6] N. Hardy, B. Dixon, J. Shapiro, and S. Hamilton, "Quantum illumination radar feasibility," presented to Emerging Technology Analytic Panel, MIT Lincoln Labs, MA, 2018.

[7] Semiconductor Industry Association. (2023, February). Global Semiconductor Sales Increase 3.3 Percent in 2022 Despite Second-Half Slowdown. [Online]. Available: https://www.semiconductors.org/global-semiconductor-sales-increase-3-2-in-2022-despite-second-half-slowdown/

[8] G. E. Moore, "Lithography and the future of moore's law," *IEEE Solid-State Circuits Society Newsletter*, vol. 11, no. 3, pp. 37–42, 2006.

[9] D. Loss, "Quantum phenomena in nanotechnology," *Nanotechnology*, vol. 20, no. 43, p. 430205, October 2009. Available: https://dx.doi.org/10.1088/0957-4484/20/43/430205

[10] S. Lopez, B. Ben, T. Hudek, D. P. Hansen, G. Eduardo, and C. J. Gronlund. (2023). Quantum Computing History and Background. [Online]. Available: https://learn.microsoft.com/en-us/azure/quantum/concepts-overview

[11] L. Ma, O. Slattery, and X. Tang, "Optical quantum memory based on electromagnetically induced transparency," *Journal of Optics*, vol. 19, no. 4, p. 043001, February 2017. Available: https://dx.doi.org/10.1088/2040-8986/19/4/043001

[12] M. Fleischhauer and M. D. Lukin, "Dark-state polaritons in electromagnetically induced transparency," *Physical Review Letters*, vol. 84, no. 22, pp. 5094–5097, May 2000. Available: https://doi.org/10.1103

[13] D. A. Steck, “Rubidium 85 d line data,” Oregon Center for Optics and Department of Physics, University of Oregon, http://steck.us/alkalidata, Tech. Rep. rev. 2.2.3, July 2021.

[14] C. Cohen-Tannoudji, B. Diu, and F. Laloë, *Quantum mechanics; 1st ed.* New York, NY: Wiley, 1977, trans. of : Mécanique quantique. Paris : Hermann, 1973. Available: https://cds.cern.ch/record/101367

[15] S. E. Harris, J. E. Field, and A. Imamoğlu, “Nonlinear optical processes using electromagnetically induced transparency,” *Phys. Rev. Lett.*, vol. 64, pp. 1107–1110, March 1990. Available: https://link.aps.org/doi/10.1103/PhysRevLett.64.1107

[16] M. Scully and M. Zubairy, *Quantum Optics* (Quantum Optics). Cambridge University Press, 1997. Available: https://books.google.com/books?id=20ISsQCKKmQC

[17] M. Fleischhauer, A. Imamoglu, and J. P. Marangos, “Electromagnetically induced transparency: Optics in coherent media,” *Rev. Mod. Phys.*, vol. 77, pp. 633–673, July 2005. Available: https://link.aps.org/doi/10.1103/RevModPhys.77.633

[18] W. W. Erickson, “Electromagnetically induced transparency,” M.S. thesis, Dept. of Mathematics and Natural Sciences, Reed College, 2012.

[19] “Ordinary electromagnetically induced transparency,” prepared notes for guided study, Dept. of Physics, Naval Postgraduate School, Monterey, CA, Winter 2013.

[20] “Time-independent perturbation theory,” class notes for Quantum Mechanics, Dept. of Physics, Naval Postgraduate School, Monterey, CA, Summer 2022.

[21] D. J. Griffiths, *Introduction to electrodynamics; 4th ed.* Boston, MA: Pearson, 2013, republished by Cambridge University Press in 2017. Available: https://cds.cern.ch/record/1492149

[22] J. Nash and F. A. Narducci, “Linear magneto-optic rotation in a cold gas,” *Journal of Modern Optics*, vol. 50, no. 15-17, pp. 2667–2675, 2003.

[23] W. Tang, B. Luo, Y. Liu, and H. Guo, “Slow light of an amplitude-modulated gaussian pulse in cesium vapor,” *IEEE Journal of Quantum Electronics*, vol. 46, no. 4, pp. 579–583, 2010.

[24] C. J. Foot, *Atomic physics* (Oxford master series in atomic, optical, and laser physics). Oxford: Oxford University Press, 2007. Available: https://cds.cern.ch/record/1080846

[25] M. M. Kash, V. A. Sautenkov, A. S. Zibrov, L. Hollberg, G. R. Welch, M. D. Lukin, Y. Rostovtsev, E. S. Fry, and M. O. Scully, “Ultraslow group velocity and enhanced nonlinear optical effects in a coherently driven hot atomic gas,” *Phys. Rev. Lett.*, vol. 82, pp. 5229–5232, June 1999. Available: https://link.aps.org/doi/10.1103/PhysRevLett.82.5229

Initial Distribution List

1. Defense Technical Information Center
   Ft. Belvoir, Virginia

2. Dudley Knox Library
   Naval Postgraduate School
   Monterey, California